Journal of Marine Research, 57, 933–966, 1999

A seasonal succession of physical/biological interaction mechanisms in the Sargasso Sea

by J. D. Wiggert[1,2], T. C. Granata[3], T. D. Dickey[4] and J. Marra[5]

ABSTRACT

Six months of concurrent, co-located physical and bio-optical time series from a moored array deployed in the Sargasso Sea during 1987 have been analyzed by combining standard Fourier analysis techniques with a unique presentation method. The spectral information obtained from the time series analysis covers four orders of magnitude in frequency space. This is especially useful for revealing temporal variations in high frequency variance and the physical/biological interactions that occur at these frequencies. The presentation method used here consists of time/frequency distributions of normalized variance and squared coherence that resulted from the time series analysis. These reveal a seasonal succession of physical/biological interaction mechanisms. It is apparent that the onset, and ongoing development, of water-column stratification initiates an evolution from a regime dominated by horizontal advection, within which phytoplankton act as a passive tracer, to one where physical processes impact the biology on spatial and temporal scales which are consonant with phytoplankton physiology. The observed interactions include: (1) transport of distinct bio-optical properties within advected mesoscale features; (2) significant phytoplankton patchiness associated with the regional evolution of the spring bloom and; (3) high frequency bio-optical variability associated with the interaction of the deep chlorophyll maximum with internal wave motions.

1. Introduction

Open ocean physical and biological processes occur over a wide range of spatial and temporal scales (Harris, 1986). At large scales, a tight correspondence between biological and physical variability is typically observed (Smith and Baker, 1985; García-Moliner and Yoder, 1994). This characteristic of pelagic systems is well documented but may lead to the erroneous perception that the biological constituents act solely as passive tracers of events within the physical environment. As the scales of physical variability approach the inherent scales of phytoplankton physiology (i.e., centimeters to meters and minutes to hours), directly ascribing bio-optical variability to specific physical or biological processes becomes less precise (Denman and Powell, 1984). Indeed, some portion of ecosystem

1. Universities Space Research Association, Greenbelt, Maryland, U.S.A.
2. Present address: ESSIC, University of Maryland, College Park, Maryland, 20742-2465, U.S.A. ***email: jwiggert@essic.umd.edu***
3. Department of Civil and Environmental Engineering and Geodetic Science, Ohio State University, Columbus, Ohio 43210-1275, U.S.A.
4. Ocean Physics Laboratory, ICESS, University of California, Santa Barbara, California, 93106-3060, U.S.A.
5. Lamont Doherty Earth Obsvervatory, Palisades, New York, 10964, U.S.A.

variability could result from a nonlinear interaction between these source terms. For instance, internal gravity wave (IGW) oscillations can produce an effective vertical diffusion of nutrients when otherwise light-limited phytoplankton are contained within a nutrient replete water parcel, resulting in enhanced primary productivity (Kahru, 1983). It is also apparent that ecosystem variability can affect physical processes. This may occur *via* biological attenuation of downwelling irradiance (Dickey and Simpson, 1983; Morel and Antoine, 1994) and observations have shown that elevated phytoplankton concentration can lead to enhanced thermal stratification which in turn increases net growth (Lewis *et al.,* 1983; Stramska and Dickey, 1994).

Within the Sargasso Sea, eddy pumping of nitrate into the euphotic zone is crucial for reconciling the difference between nitrate concentrations prior to the spring bloom and geochemical estimates of annual new production (McGillicuddy *et al.,* 1998). Eddies in this region typically have horizontal scales of $O(100\ \text{km})$ and vertically homogeneous physical properties through at least 400 m (Joyce, 1984). Both cold-core (cyclonic) and warm-core (anticyclonic) rings are prevalent (Nelson *et al.,* 1989; McGillicuddy *et al.,* 1999). Superposition of eddy-based bio-optical properties on the seasonal evolution consisting of wintertime nitrate entrainment followed by poleward propagation of the spring phytoplankton bloom and summertime oligotrophic conditions in the surface waters results in significant phytoplankton patchiness over much of the year (Hitchcock *et al.,* 1985; Siegel *et al.,* 1999). The distinct physical properties associated with both cyclonic and anticyclonic rings that advect into and throughout the region, result in eddy bio-optical properties that are easily distinguishable from the ambient waters (Wiggert, 1995; McNeil *et al.,* 1999).

At scales below those associated with mesoscale dynamics, *in-situ* studies reveal decreasing coherence between physical and biological variables. Power spectra determined from coincident temperature and chlorophyll spatial series show a break in spectral slope at 100–400 m which corresponds to reduced coherence for smaller phytoplankton patch scales (Denman, 1976; Fasham and Pugh, 1976; Platt, 1977). The maximum horizontal wavelength associated with an IGW field is $O(10^2–10^3\ \text{m})$. Thus, IGW length scales coincide with the observed break in spectral slope and the decay of coherence between physical and biological signals. This transition coincides with the biological constituents' shift from passive transport within a mesoscale dominated physical regime to direct interaction with high frequency environmental fluctuations within an internal wave dominated physical regime. In other words, the dominant physical/biological interaction mechanism evolves from advectively- to locally-derived phytoplankton patchiness.

In the context of seasonal evolution for temperate water ecosystems, the transition to the latter interaction mechanism coincides with the permanent shoaling of the mixed layer and the associated spring phytoplankton bloom. This spring bloom is triggered when the mixing depth becomes less than the critical depth (Sverdrup, 1953; Mann and Lazier, 1991). The shoaling of the mixed layer also signifies initiation of the seasonal evolution of near-surface water column stratification. This stratification is necessary for supporting the

IGW field below the mixed layer and helps establish the deep chlorophyll maximum (DCM). Here we apply the hypothesis that as nutrients become limiting within the mixed layer, the DCM develops, persists and subsides primarily in response to the most advantageous balance between light intensity and nitrate availability resulting from turbulent mixing (Jamart *et al.,* 1977; Varela *et al.,* 1992). Due to the correspondence in their characteristic temporal and spatial scales, the superposition of a coincidentally developing IGW field suggests a direct interaction with the evolution of the DCM.

Internal tide and internal wave amplitudes of 10–20 m are typically observed with up to one third of total IGW band (Δf_{IGW}) variance associated with the semi-diurnal tide (Gregg and Briscoe, 1979; Denman and Gargett, 1983). Since downwelling solar irradiance attenuates exponentially, oscillations of this magnitude lead to significant variations in photosynthetically available radiation (PAR). In fact, 100-fold variations in PAR, associated with IGW oscillations, have been observed (Haury *et al.,* 1983). Since phytoplankton physiological response can be shorter than the vertical oscillation period, the associated irradiance fluctuations can result in instantaneous photosynthetic rates that are a complex function of cell light history (Marra, 1978; Lewis *et al.,* 1984; Denman and Marra, 1986; Prezelin *et al.,* 1991). Modeling studies suggest that this interaction can significantly enhance near-surface phytoplankton growth rates and substantially impact phytoplankton biomass and patchiness (Kamykowski, 1974; Holloway, 1984; Lande and Wood, 1987; Holloway and Denman, 1989; Franks and Marra, 1994).

In this paper, we report on a seasonal evolution of physical/biological interactions observed in the Sargasso Sea. High-resolution physical and bio-optical time series were coincidentally sampled from moored sensors for nearly 10 months encompassing three oceanic seasons. Data were divided into six periods, based on distinct physical/biological interactions (Table 1). Two previous reports defined similar periods and contain considerable supplementary information (Dickey *et al.,* 1991; 1993). Spectral variance and coherence between a given pair of variables were calculated by applying fast Fourier transforms (FFTs) and associated time series analysis techniques. Deployment-averaged power spectra revealed that variance, at all frequencies, was time-dependent (Wiggert, 1995). This motivated the development of a means of illustrating the temporal evolution of variance within these measurements and resulted in the time-frequency maps that we present. The dominant features captured in the evolution of the lowest resolved frequencies are consistent with mesoscale processes readily distinguished within the time series. Changes in variance at higher frequencies that were not discernible within the time series, became apparent using the time-frequency maps. This analysis provides especially tantalizing evidence that the internal wave field supports the development and persistence of the DCM. Overall, these maps provide a new perspective on the seasonal evolution of oceanographic processes and their interactions.

We begin with a brief summary of the mooring experiment, followed by a description of the time-frequency analysis, and the terminology associated with the time-frequency maps. The results report the features in the spectral variance and coherence maps for each period.

Table 1. A synopsis of the dominant interaction mechanism for each of the six periods defined within the text. Each period's temporal extent is defined in Julian day and with calendar day. The double line between P3 and P4 denotes the interdeployment break in the time series. The mean current velocity at 62 meters, mixed layer depth (Z_{ML}) and euphotic zone depth (Z_{EU}) are given. Daily estimates for Z_{ML} and Z_{EU} were linearly interpolated from the mid-day profile of temperature and log(PAR) based on the eight MVMS depths. The criterion for defining Z_{ML} was a ΔT of 0.1 °C from the surface temperature. Z_{EU} was taken as the 1% light level. The listed error estimates are based on one standard deviation for each period's set of daily estimates. The asterisk (*) denotes mean values for which some estimates of Z_{ML} or Z_{EU} were obtained by extrapolating beyond the deepest instrument (160 m).

Period (JD)	Speed (cm/s)	Z_{ML} (m)	Z_{EU} (m)	Physical/Biological Interaction Mechanism
P1 (70–78) 11–19 March	40 ± 17	137 ± 37*	107 ± 14	Strong HKE. Advected waters transporting distinct bio-optical characteristics. Alternating between intensive mesoscale activity and deep convection.
P2 (78–90) 19–31 March	19 ± 9	138 ± 42*	143 ± 62*	Extended period of deep convection and lower HKE followed by onset of permanent stratification corresponding with spring bloom. Differential horizontal stratification results in significant phytoplankton patchiness.
P3 (90–130) 31 March–10 May	48 ± 20	24 ± 17	72 ± 8	Strong HKE. Developing IGW field. Strong temporal correspondence between observed onset of $G_N(\Delta f_{IGW})$ in temperature and Chl. Superposition of variability due to mesoscale advection and patchiness associated with spread of Sargasso Sea's spring bloom.
P4 (135–185) 15 May–4 July	10 ± 5	16 ± 4	105 ± 6	Some far field mesoscale interaction. IGW field strongly associated with both Δf_M and Δf_{IGW} Chl variability. Temp/Chl $\gamma_{XY}(\Delta f_{IGW})$ indicative of nitrate driven primary productivity and developing DCM.
P5 (185–220) 4 July–8 August	24 ± 16	16 ± 5	123 ± 7	Sharp mesoscale front associated with cold-core ring and Gulf Stream outbreak. Vertical nitrate transport occurs at warm side of front due to near-inertial internal wave intensification. Strong IGW field dissociated with Chl variability due to intensified submixed layer stratification that inhibits vertical diffusion of nitrate.
P6 (220–240) 8–28 August	9 ± 6	18 ± 5	123 ± 8	IGW field at 62 m no longer directly associated with Chl variability. This indicates stochastic nature of primary productivity driven by regenerated nutrients and continued subsidence of DCM. Episodic bloom associated with shear-induced mixing and injection of nitrate from deeper waters.

In the discussion we interpret observations pertaining to the seasonal evolution and its disruption by mesoscale activity. Additionally, the time-frequency maps instigate a detailed look at 5-day time series subsections that aid our characterization of the DCM's seasonal evolution. Lastly, we conclude that our analysis provides new insights and perspectives on the seasonal evolution of physical/biological interactions as well as phytoplankton patchiness in an oligotrophic ecosystem.

2. Methods

The time series measurements used for this analysis were acquired during the 1987 Biowatt experiment by the Multi-Variable Moored System (MVMS). They consist of four minute resolution physical and bio-optical measurements obtained by a mooring in the oligotrophic waters of the Sargasso Sea (34°N, 70°W) (Dickey *et al.,* 1991). The variables used here consist of zonal and meridional current, temperature, stimulated fluorescence and beam transmission. Detailed descriptions of the data and the methods used to transform stimulated fluorescence to chlorophyll-fluorescence (Chl) and beam transmission to beam attenuation coefficient (C_{660}) are discussed elsewhere (Dickey *et al.,* 1991). Measurements were made at eight depths over the upper 160 m of the water column and, through the use of three successive deployments, included parts of all four oceanic seasons. The present analysis is limited to the Biowatt mooring's first two deployments. Data from the third deployment were the focus of related work which discussed episodic biomass increases within the DCM coinciding with nutrient injections associated with downward propagating near-inertial wave packets (Granata *et al.,* 1995).

Combining high resolution with an extended sampling period (260 d) provided an opportunity to study numerous physical and biological processes (e.g., mesoscale eddies, tidal and inertial motions, episodic phytoplankton blooms, diel cycles, and IGW) and their interactions. FFTs performed on 8192 point (23.8 d) ensembles produced variances for frequencies from mesoscale ($O(10^{-1}$/d)) through the IGW ($O(10^{3}$/d)). Ensembles were overlapped by 75%, resulting in a 5.7 day displacement between the mid-point of adjacent ensembles. Before applying the FFT, the mean was removed and each ensemble was detrended and cosine tapered to insure periodicity. This choice of tapering window was based on its shape (i.e., width of the main lobe versus relative magnitude and falloff of the side lobes) in frequency space (Harris, 1978). Following application of the FFT, the results were re-colored to preserve total variance. Finally, WKB scaling was applied to the spectral result for each ensemble in order to allow for intercomparison between variance estimates within the IGW band (Leaman and Sanford, 1975; Eriksen, 1988).

a. Temporal distributions of normalized spectral variance: Development and interpretation

Temporal variations in spectral variance are presented in time-frequency maps which show normalized spectral density ($G_N(f, t)$) as a function of frequency and time for a given

variable. Normalization consists of dividing each individual autospectrum by the mean autospectra for all ensembles represented within the map. This process has been defined as

$$G_N(f, t_o) = \frac{G_{xx}(f, t_o)}{\langle G_{xx}(f) \rangle}, \tag{1}$$

where $G_{xx}(f, t_o)$ is the standard autospectral density function (Bendat and Piersol, 1986) for a given ensemble centered on $t = t_o$. The mean autospectrum has been defined as

$$\langle G_{xx}(f) \rangle = \frac{1}{N_s} \sum_{1}^{N_s} G_{xx}(f, t), \tag{2}$$

where N_s is the number of autospectra in the average. This normalization detrends each autospectrum by removing the "red" behavior typical of oceanic power spectra (i.e., monotonically decreasing spectral power with increasing frequency) since variance at a given frequency is normalized by the mean variance at that frequency. This normalization has a similar effect on normally prominent tidal, inertial and diel peaks which are not significant features within the $G_N(f, t)$ maps. In general, the gray scale only represents $G_N(f, t)$ values >1.0 (i.e., above average). This serves to highlight energetic periods. However, in the case of the temperature $G_N(f, t)$ maps, isolines of 0.05 and 0.5 are used to illustrate development of the IGW field.

b. Temporal distributions of spectral coherence: Calculation and determination of statistical significance

To quantify linear inter-relationships between two variables, coherence between time series ($\gamma_{XY}(f, t)$) was determined through the use of cross-spectral density functions ($G_{XY}(f, t)$, Bendat and Piersol, 1986). Standard statistical methodology was applied to determine the level of statistically significant coherence (Bloomfield, 1976). This depends on the confidence interval (95%) and the degrees of freedom (≥ 6). In this case, the latter depends on the symmetry of the Fourier transform in frequency space and the number of points included in band averaging (≥ 3). This value is at its minimum within the mesoscale band and increases with frequency at intervals chosen not to obscure prominent features in the autospectra, such as tidal and inertial peaks (Dickey *et al.,* 1991; Wiggert, 1995). To make discussions of significant coherence between fields straightforward, $\gamma_{XY}(f, t) = 0.6$ is used as the gray scale threshold (i.e., $\gamma_{XY}(f, t) < 0.6$ is statistically insignificant).

c. Time and frequency representations on the G_N and γ_{XY} distributions

The G_N and γ_{XY} distributions exist in time-frequency space, although specific reference to time has been dropped and is assumed (i.e., $G_N(f) \equiv G_N(f, t)$). Each map's time domain (ordinate axis) is given in Julian Day on the left side, with a visual representation of the six defined periods (Table 1) on the right side. Each map's frequency domain (abscissa)

consists of a linear scale representing log transformed frequency (in cycles per day (cpd), where 0.0 corresponds to 1/day) on the bottom and a visual representation of the mesoscale (Δf_M) and internal gravity wave (Δf_{IGW}) bands along the top. The diurnal (f_D), semi-diurnal (f_{SD}) and inertial frequencies (f_I), are provided as additional reference points. The mesoscale band is defined as 1 to 11 days while the internal wave band ranges from the inertial frequency to the Brunt-Väisälä frequency ($f_I - f_N$), though in our study f_N is attainable only during periods of deep convection (Wiggert, 1995). However, the reader should note that at such times, the frequency range of the internal wave band depicted on these maps is inaccurate since these physical conditions will not support an internal wave field. Finally, while data acquisition started on Julian Day (JD) 60, the time lines presented here start 10 days later, since the initial time is based on the temporal mid-point of the first FFT ensemble. While most maps span JD 70–240, fluorometer biofouling reduced the period of maps based on Chl measurements. These occurrences have been noted in the figure captions and can be identified by the period representations along the right side.

d. Nomenclature and interpretation

Working with these maps has necessitated the development of nomenclature designed to enhance brevity. For instance, temperature $G_N(\Delta f_M)$ refers to the normalized temperature variance (G_N) for the mesoscale band (Δf_M). Similarly, temperature and Chl $\gamma_{XY}(\Delta f_{IGW})$ refers to the coherence (γ_{XY}) between temperature and chlorophyll-fluorescence for the internal wave band (Δf_{IGW}). Individual characteristic frequencies (i.e., f_D, f_{SD} and f_I) are differentiated from frequency *bands* that are defined within the text (i.e., Δf_M and Δf_{IGW}) by the Δ symbology. Finally, throughout this analysis we equate significant coherence between individual velocity components and scalar properties with horizontal advection. This interpretation is analogous to studies of turbulence in fluids where the mean and fluctuating parts of time series observations are partitioned and net transport is related to the skewness of the observed properties' probability distribution (Townsend, 1976). This is quantified using the cross-spectrum, which is incorporated within the coherence calculation that we present.

3. Results

a. Period 1 (JD 70–78)

Period 1 was dominated by eddy-driven advection (Fig. 1a). While the currents are generally directed toward the south with speeds of 40–50 cm/s, sufficient fluctuations in speed and directional veering were present to result in elevated current $G_N(\Delta f_M)$ at all depths (Figs. 2a and 3). Mesoscale activity is also evident in time series of temperature, which shows significant oscillations that are reflected within Z_{ML}, which alternates between uncharacteristically shallow depths (30–50 m) and deep convection (>160 m, Figs. 2b and 4). Periods of shallow Z_{ML} relate to warm Gulf Stream outbreaks (Cornillon *et al.,* 1986) that disrupt the deep wintertime convective mixing (Fig. 2b). Temperature $G_N(\Delta f_M)$

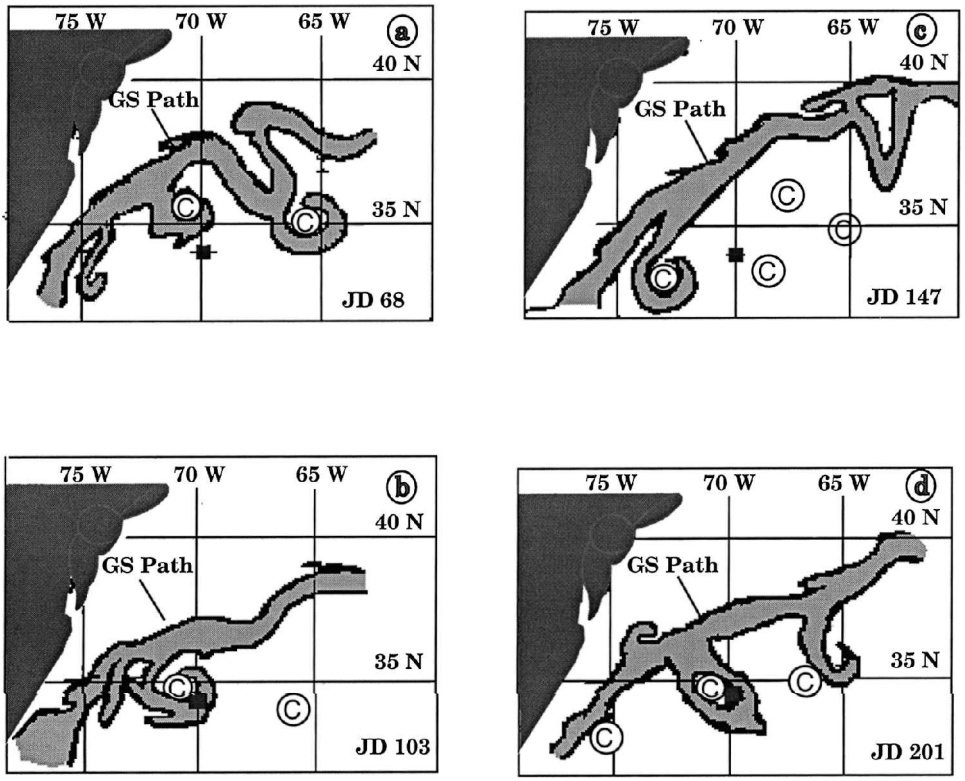

Figure 1. Synoptic maps of sea surface temperature for the region. The mooring site (34N 70W) is indicated (■). The date for the map is given. These maps provide synoptic information for four of the six periods defined within the text. The track of the Gulf Stream (GS Path) is shown and the cold core rings (C) are indicated.

reflects these Z_{ML} excursions most prominently near the surface and is elevated throughout the water column (Figs. 4 and 5). Based on $\gamma_{XY}(\Delta f_M)$ between currents and temperature, the advection of heat associated with these outbreaks is predominantly zonal (Fig. 6). Euphotic zone depth (Z_{EU}) ranges from 80 m to 130 m, indicating low biomass but high variability (Fig. 4). These variations in optical clarity appear as elevated C_{660} $G_N(\Delta f_M)$ and are directly associated with the Z_{ML} fluctuations (Figs. 4, 7a). They also appear, though less prominently, as elevated Chl $G_N(\Delta f_M)$ at both 62 m and 101 m (Figs. 7b and 7d). Zonal transport of bio-optical properties is not indicated in $\gamma_{XY}(\Delta f_M)$ between the currents and bio-optical variables below 62 m (Figs. 8 and 9). However, in keeping with the direction of advected heat, it is apparent at 23 m in $\gamma_{XY}(\Delta f_M)$ between currents and C_{660} (not shown). This evidence suggests the passage of a succession of water masses associated with either deep wintertime convection or Gulf Stream outbreaks.

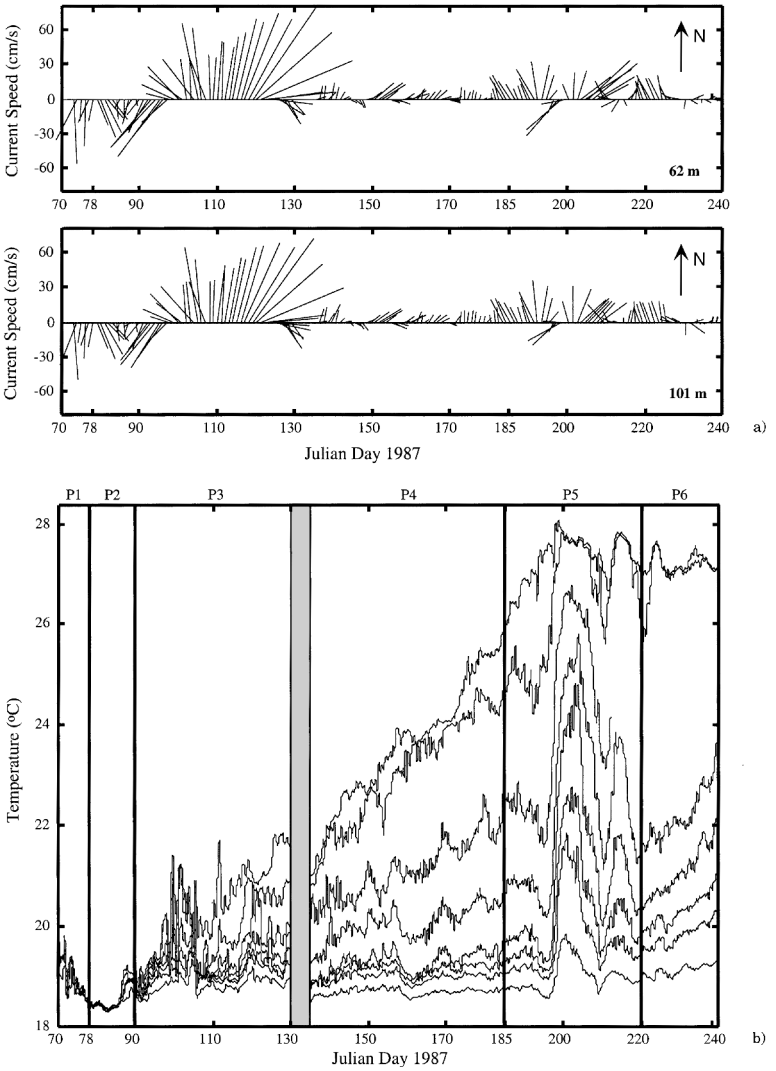

Figure 2. (a) Current stick plots from 62 and 101 m. The directional definition also indicates a value of 50 cm/s. (b) Stacked temperature time series from all MVMS depths. The time axis and the period demarcations are shown. The break between MVMS deployments occurs between P3 and P4.

b. Period 2 (JD 78–90)

Period 2 had current speeds less than half those observed during periods 1 and 3 (Table 1) and an uninterrupted deep mixed layer (>160 m, Fig. 4). These physical properties appear as significant reductions in both current and temperature $G_N(\Delta f_M)$ at all depths (Figs. 3 and 5). Additionally, $\gamma_{XY}(\Delta f_M)$ between these variables indicates negligible

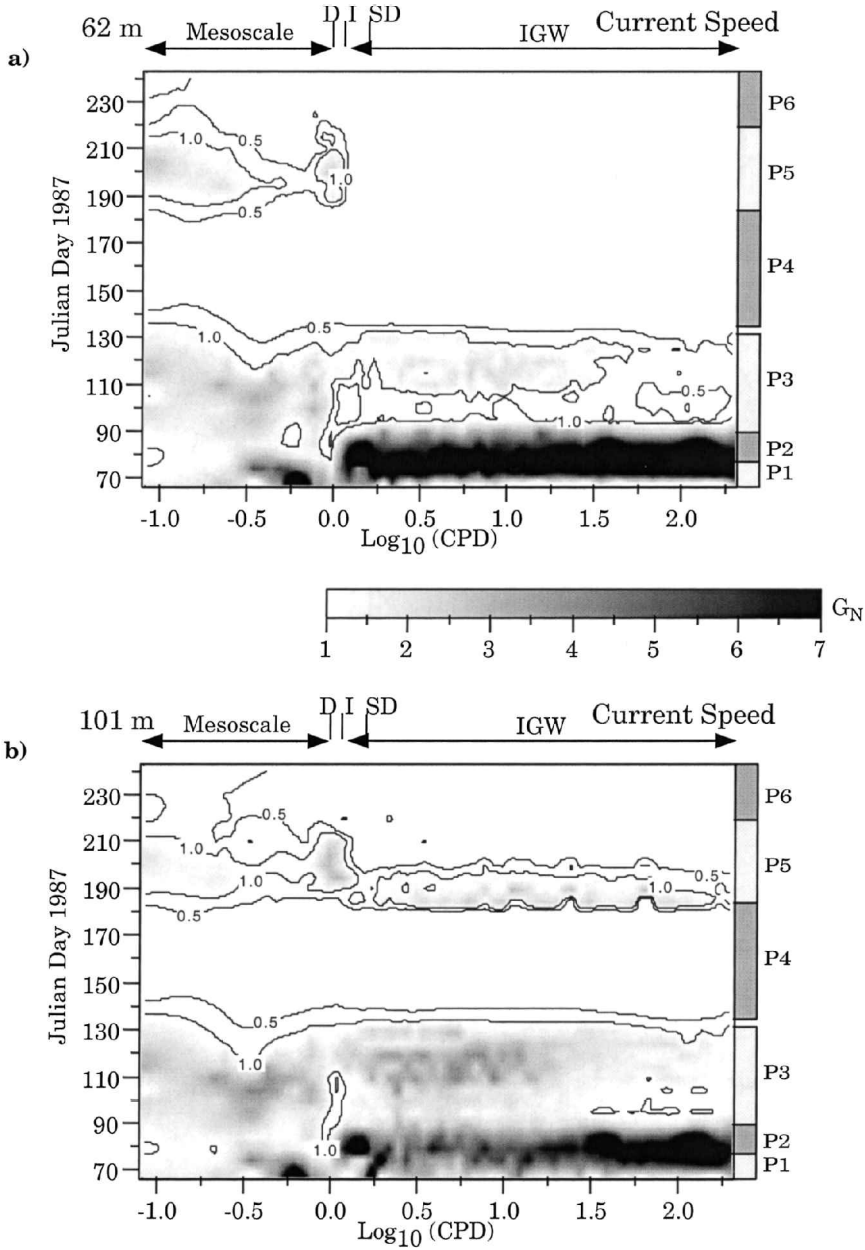

Figure 3. Current $G_N(f)$ from 62 and 101 m. The frequency axis is partitioned into two main parts consisting of the mesoscale band (Δf_M) and the internal gravity wave band (Δf_{IGW}). The diurnal (f_D), inertial (f_I) and semi-diurnal (f_{SD}) frequencies are shown. This partition is indicated on all of the G_N and γ_{XY} images (see Figs. 5–9). The time line is indicated on the left of each plot. The period boundaries are also indicated on the right side of each plot. Generally, these images cover all six periods. However, bio-optical data return did not always allow for covering all six periods. These exceptions are noted in the caption for the particular figure.

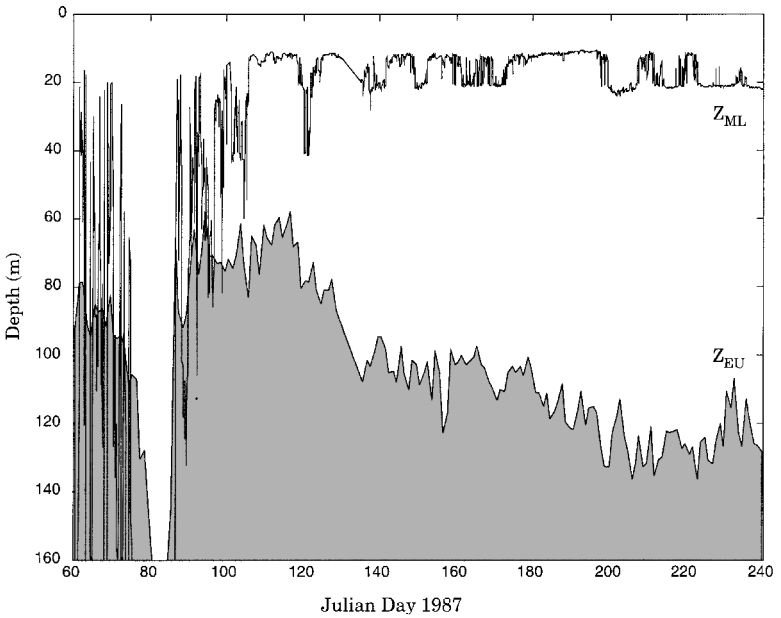

Figure 4. Time series of daily averaged mixed layer depth (Z_{ML}) and euphotic zone depth (Z_{EU}). Z_{ML} is determined using a 0.1°C difference from the measured surface temperature. Z_{EU} is defined as the 1% light level. This is determined daily by applying a one hour data window, centered on noon, to the moored PAR time series. The points obtained for each sensor are used to create a vertical profile from which the depth of 1% light is estimated.

advective heat transport (Fig. 6). This evidence indicates reduced mesoscale activity near the mooring, which is supported by synoptic maps of SST and sea-surface height (Dickey *et al.,* 1993). Values of 23 m C_{660} $G_N(\Delta f_M)$, 62 m Chl $G_N(\Delta f_M)$, and to a lesser degree at 81 m and 101 m, are all elevated (Fig. 7). Additionally, $\gamma_{XY}(\Delta f_M)$ between zonal current and Chl indicates phytoplankton patch transport throughout this period (Fig. 8a). The lack of specific water mass transport coupled with the elevated bio-optical variance indicates significant phytoplankton patchiness in waters with relatively homogeneous physical properties.

Over the last three days of this period, reduced current velocities persist while an abrupt reduction in Z_{EU} and Z_{ML} is observed (Fig. 4), in conjunction with an episodic increase in biomass seen in C_{660} time series over the upper 40 m (Dickey *et al.,* 1991). This jump in biomass leads to the noted increase in C_{660} $G_N(\Delta f_M)$ and Chl $G_N(\Delta f_M)$ (Fig. 7). Since surface short wave insolation was 90% lower than values measured before and after this phytoplankton 'bloom,' it is likely that this feature was advected through the mooring site and not locally generated. $\gamma_{XY}(\Delta f_M)$ of Chl with temperature appears at a frequency which corresponds well with this bloom's temporal extent of about 2 days (Fig. 9), while the current measurements indicate that this bloom was transported over the moored array from the north (Fig. 2a).

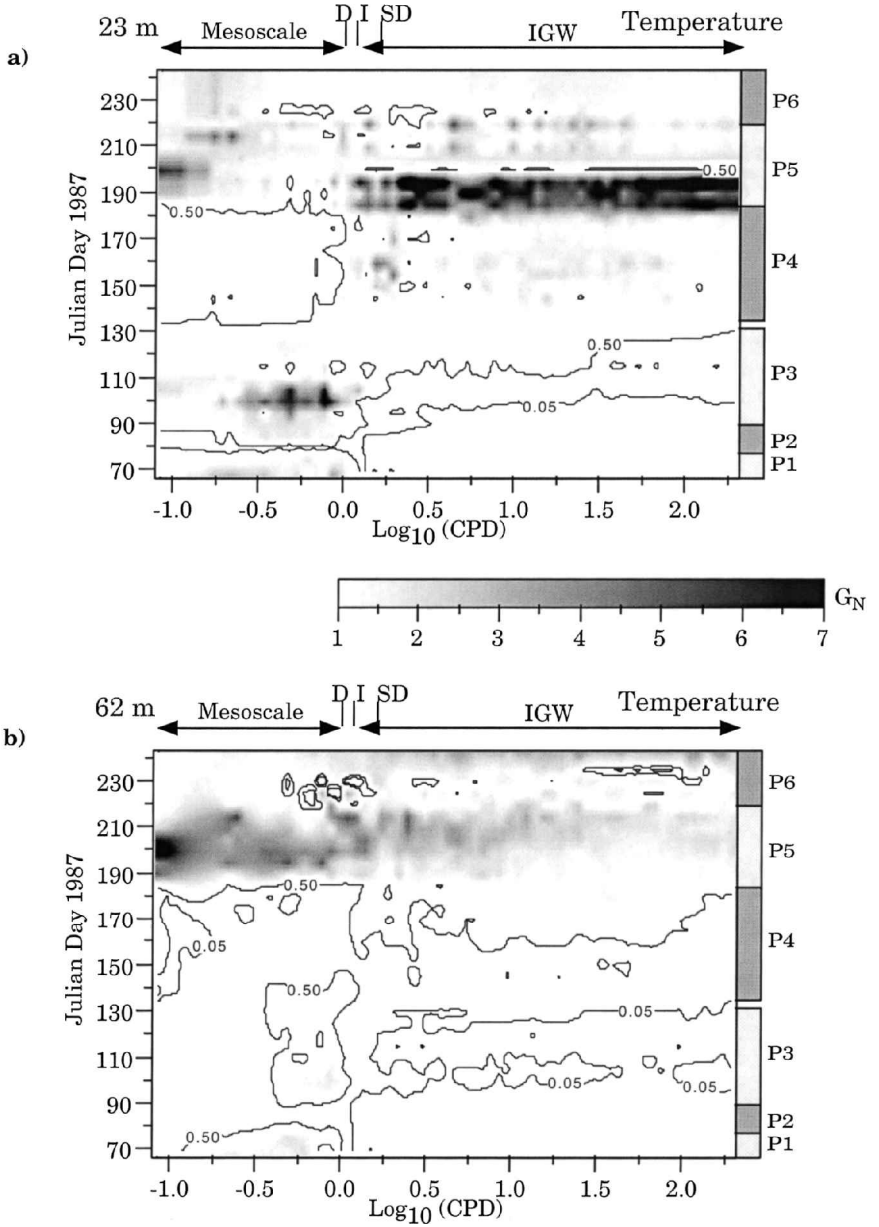

Figure 5. Temperature $G_N(f)$ from 23, 62, 81 and 101 m. Isolines of $G_N = 0.05$ and $G_N = 0.5$ are indicated to emphasize correspondence between the development of Δf_{IGW} variability in temperature and the onset of Δf_{IGW} variability in the bio-optical data (Fig. 7).

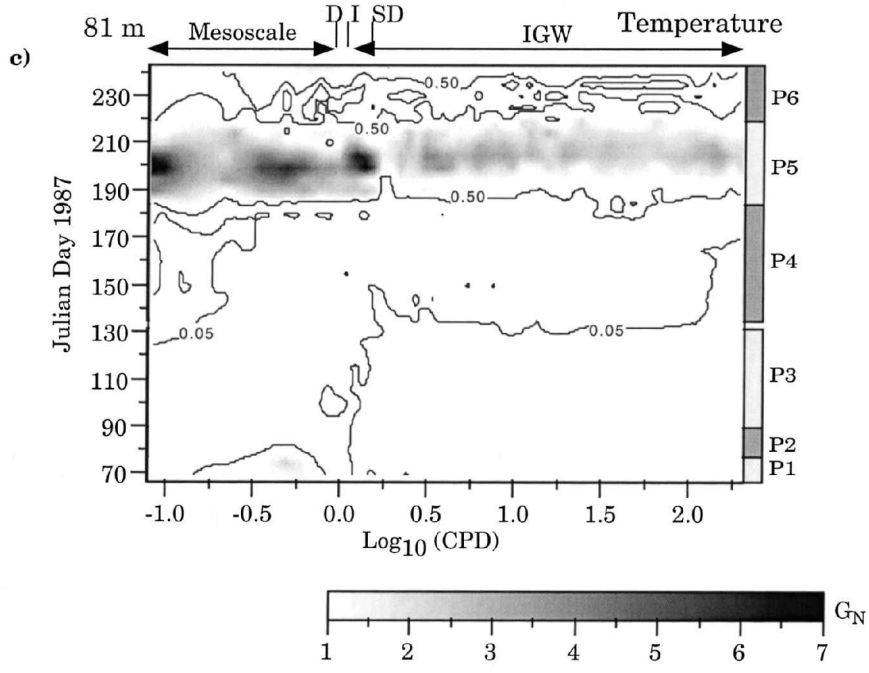

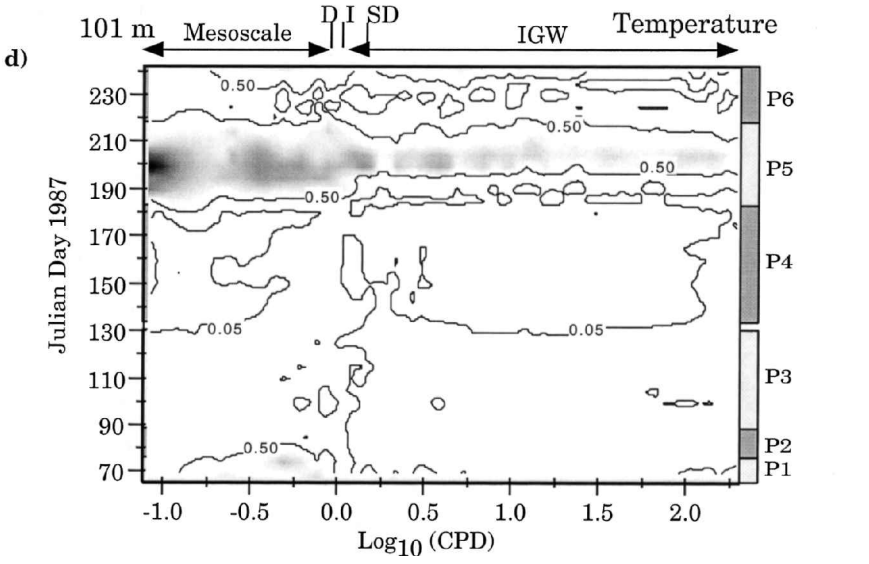

Figure 5. (Continued)

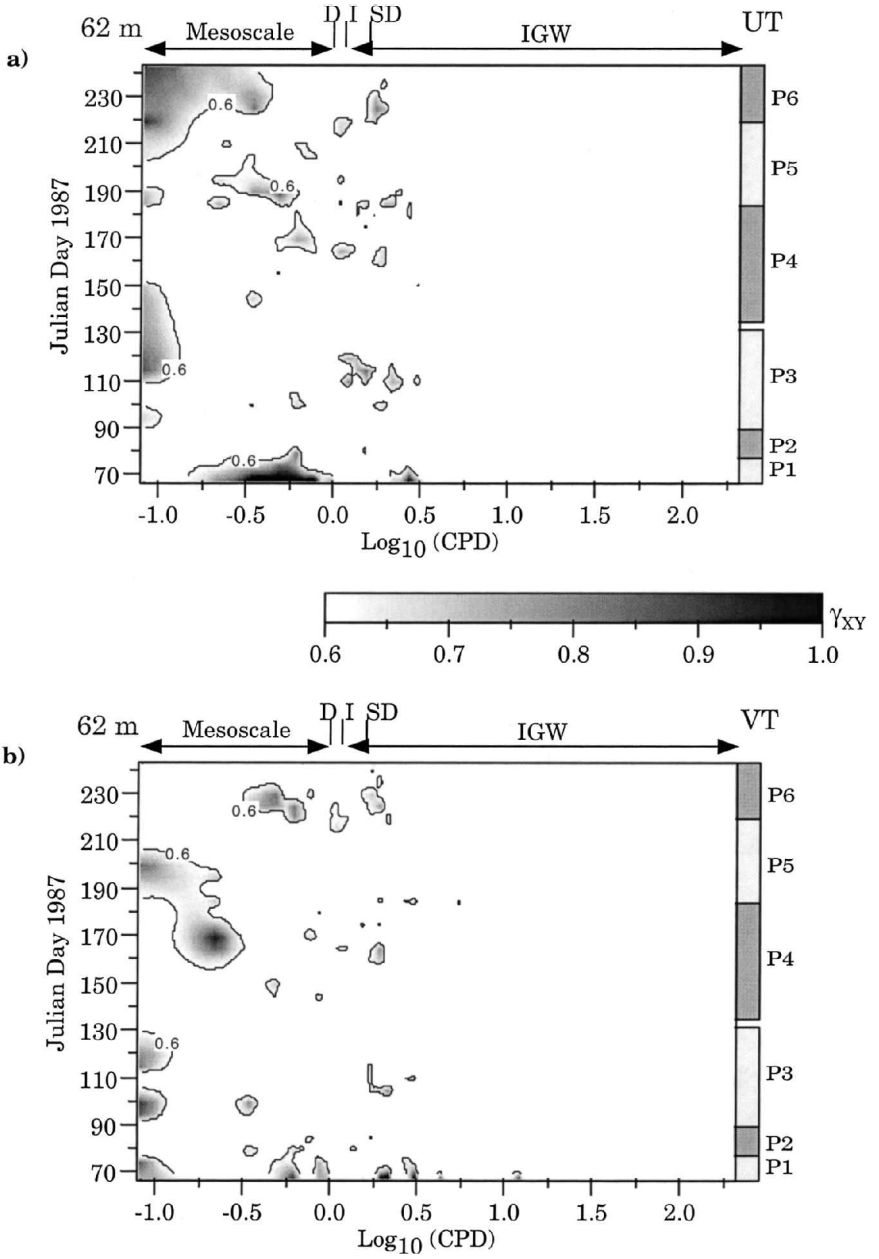

Figure 6. $\gamma_{XY}(f)$ between temperature and the individual current directions at 62 and 101 m.

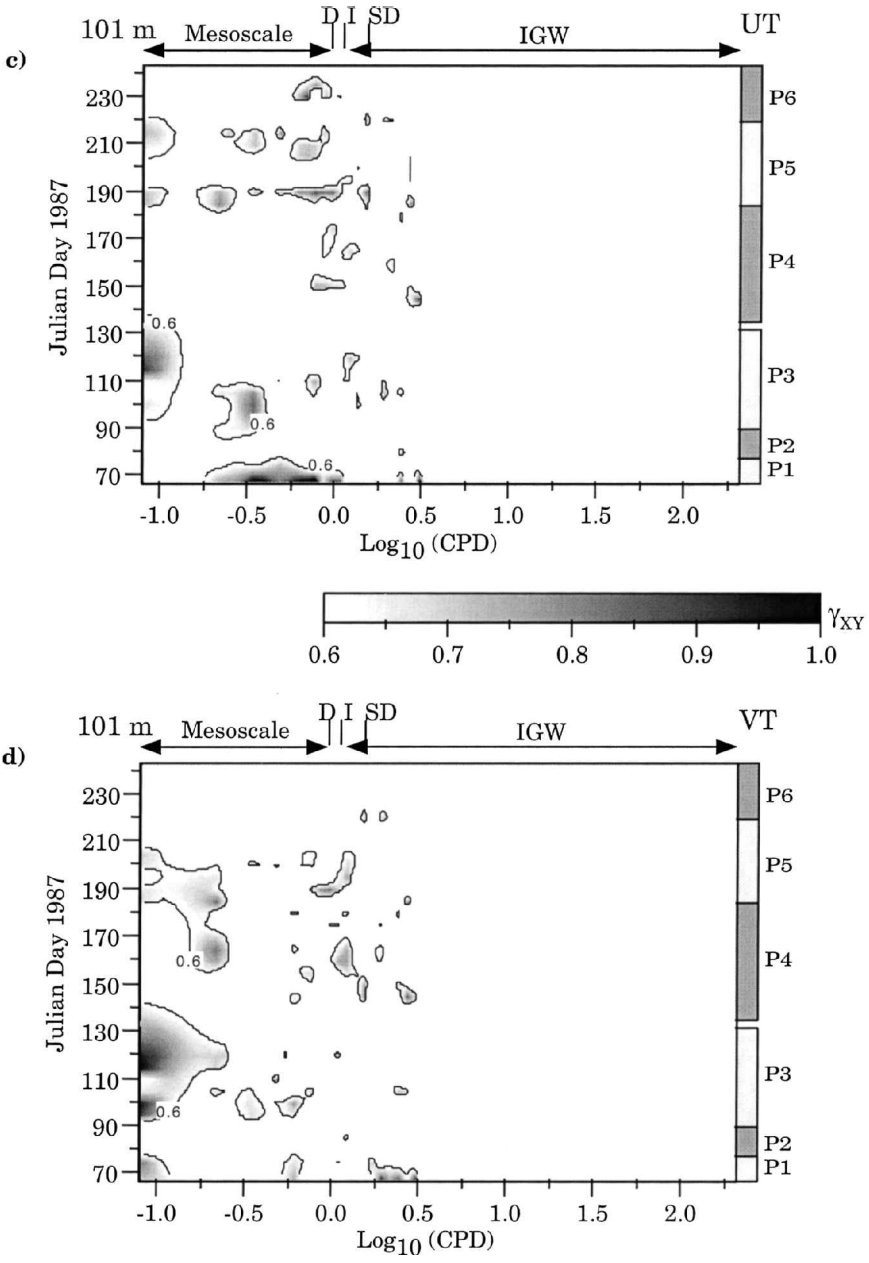

Figure 6. (Continued)

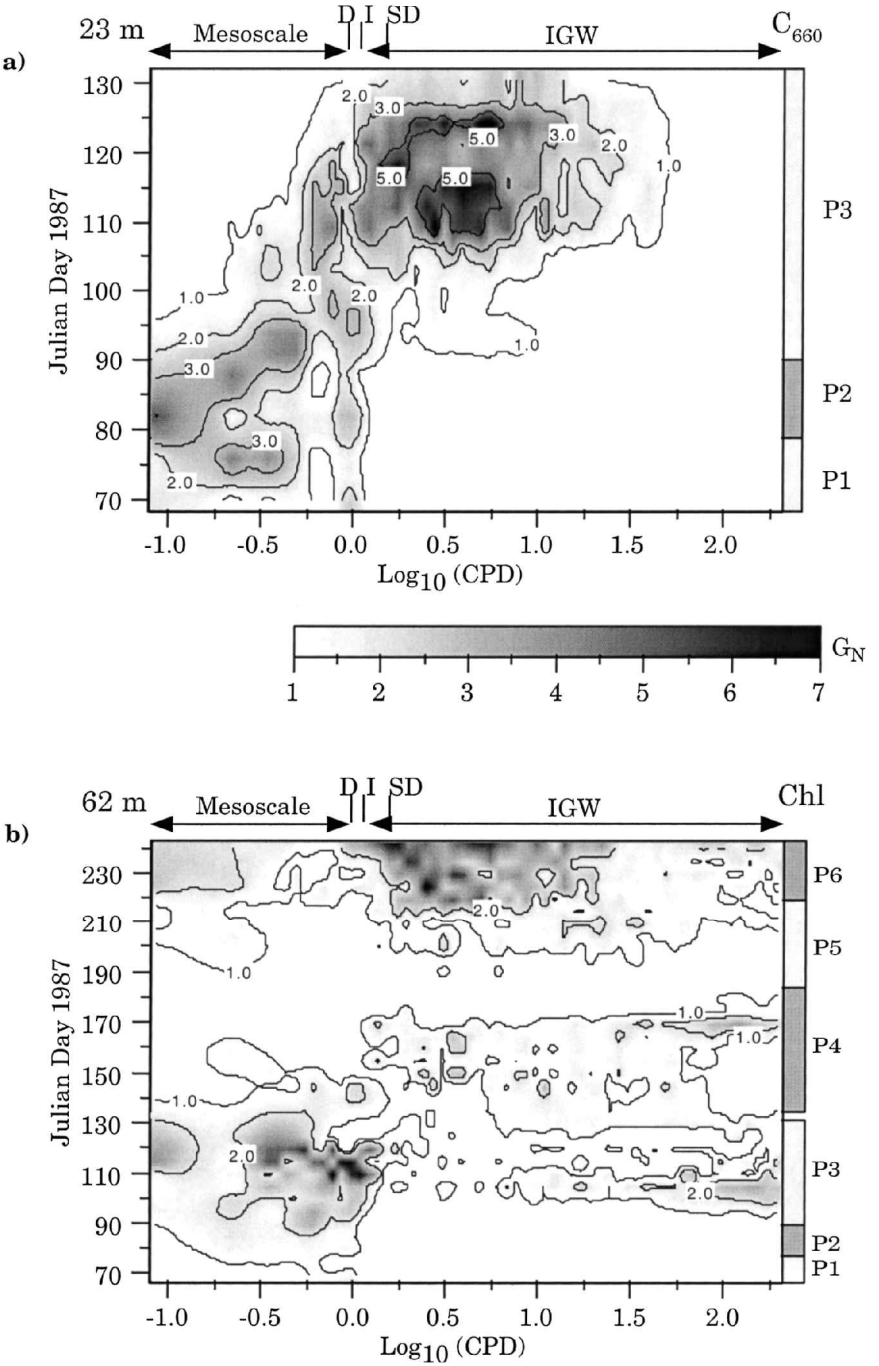

Figure 7. Bio-optical $G_N(f)$. Map a is of C_{660} from 23 m over the first three periods. Maps b–d are of Chl from 62, 81 and 101 m, respectively. The 101 m record (7 d) is shortened due to bio-fouling.

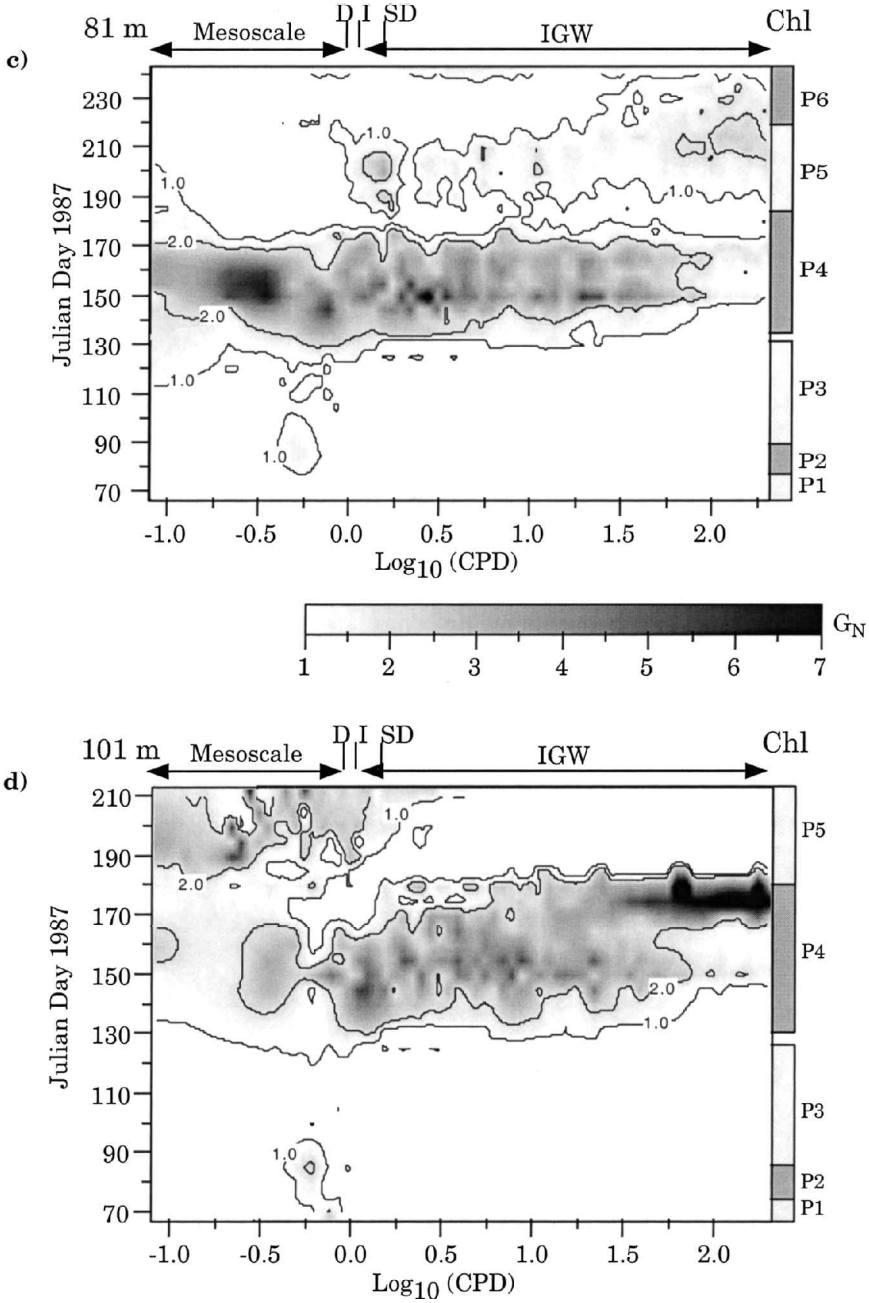

Figure 7. (Continued)

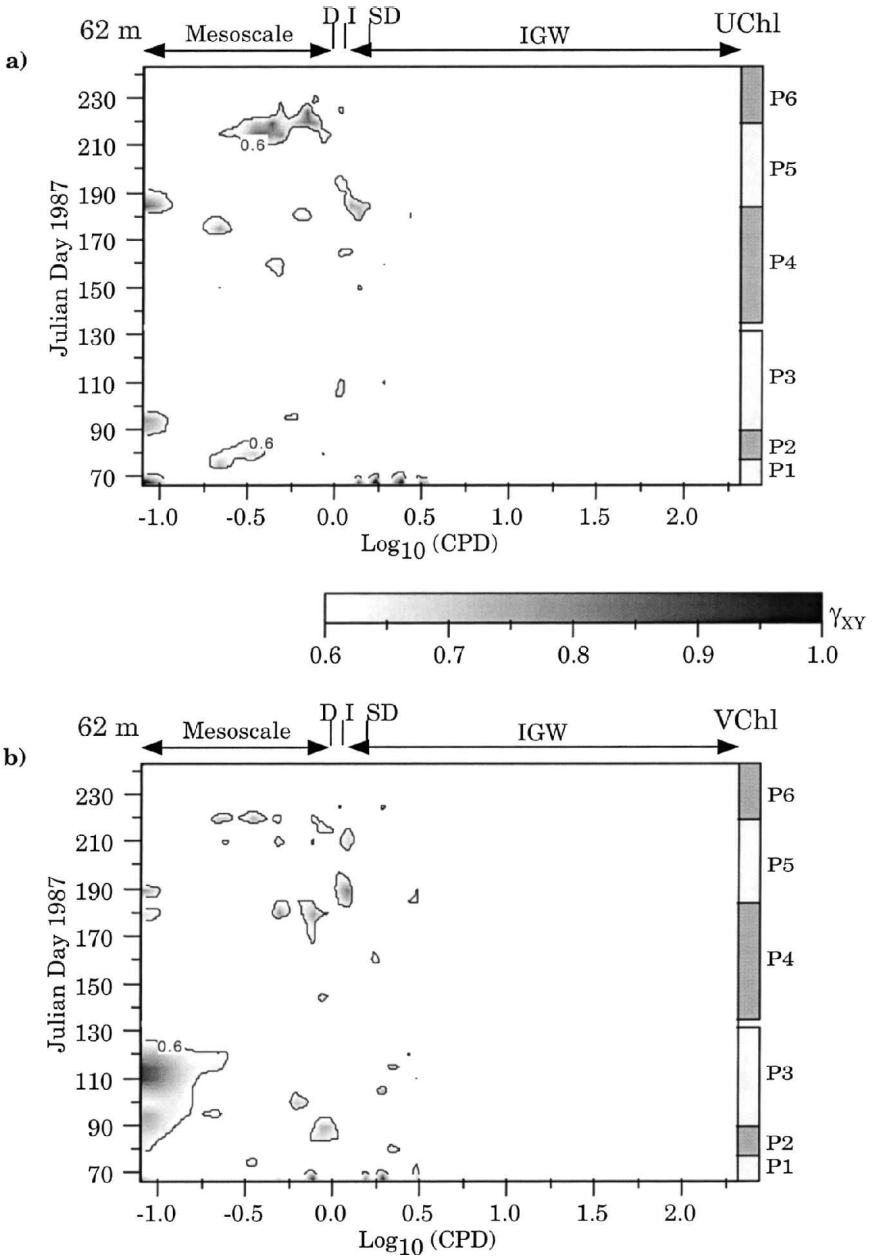

Figure 8. $\gamma_{XY}(f)$ between currents (U, V) and Chl from 62 m.

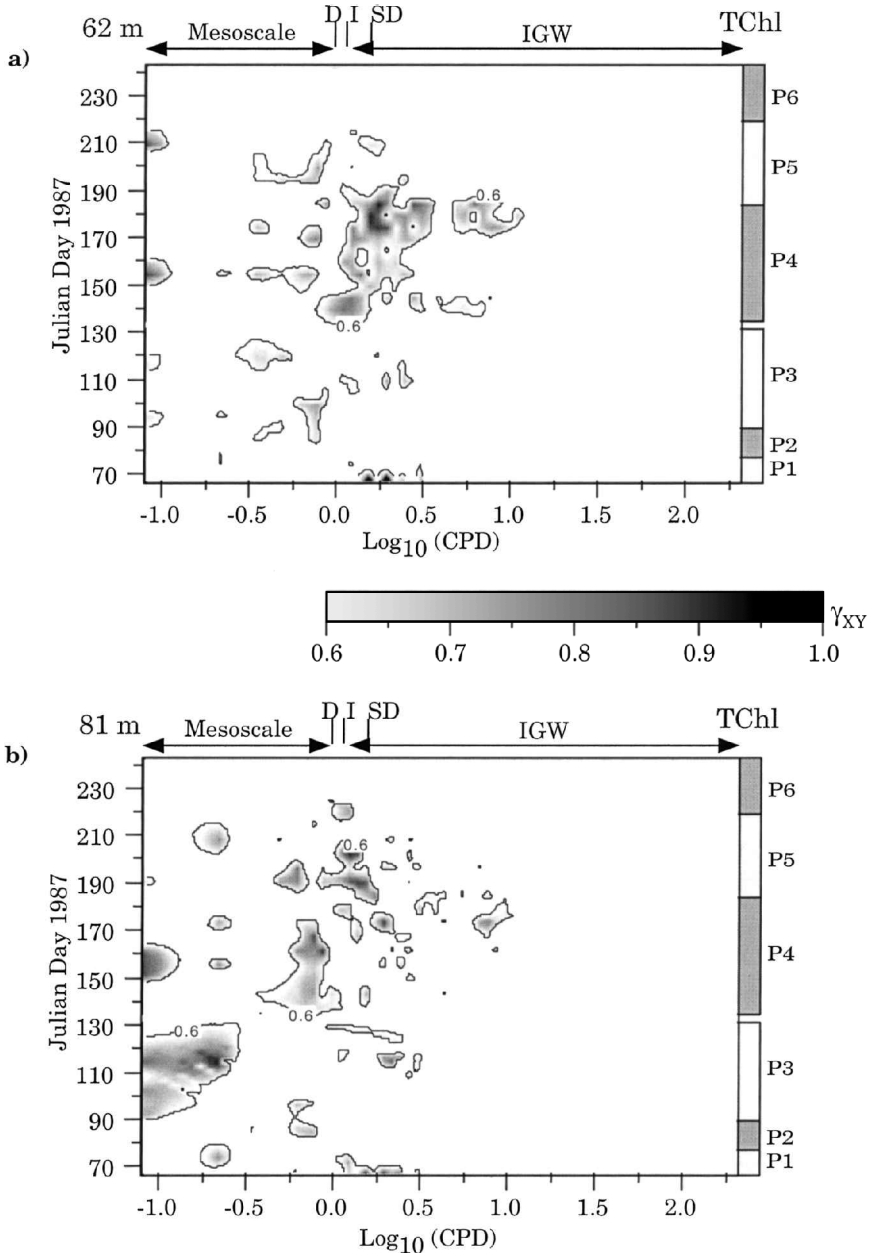

Figure 9. $\gamma_{XY}(f)$ between temperature and Chl from 62 and 81 m.

c. Period 3 (JD 90–130)

Period 3 was dominated by strong advection driven by the consistent presence of a cold-core eddy north of the mooring (Fig. 1b). The eddy drives the observed current speeds (up to 125 cm/s) and the pronounced directional veering (Fig. 2a, Table 1), represented in current $G_N(\Delta f_M)$ (Fig. 3). Temperature $G_N(\Delta f_M)$ does not reflect this mesoscale activity below the mixed layer (Fig. 5). However, $\gamma_{XY}(\Delta f_M)$ of currents with temperature at both 62 m and 101 m does indicate horizontal transport of distinct waters (Fig. 6). Additionally, while C_{660} $G_N(\Delta f_M)$ remains >1 within some part of Δf_M but decreases throughout the period, Chl $G_N(\Delta f_M)$ increased with a more pronounced expression at 62 m than at 81 m (Figs. 7a–c). Maps of $\gamma_{XY}(\Delta f_M)$ between meridional current and Chl at 62 m and between temperature and Chl at 81 m (Figs. 8b and 9b), indicate predominantly meridional transport of bio-optical properties by the eddy-driven flow field. Finally, while the appearance of elevated current $G_N(\Delta f_M)$ is uniform with depth, elevated C_{660} $G_N(\Delta f_M)$ and Chl $G_N(\Delta f_M)$ appear later with depth (Figs. 3 and 7).

Permanent stratification and the ensuing evolution of the seasonal thermocline initiate during period 3 and support the seasonal intensification of the upper ocean internal wave field. This intensification is represented in temperature $G_N(\Delta f_{IGW})$ by the 0.05 and 0.5 isolines (Fig. 5). At 23 m, the 0.05 isoline in temperature $G_N(\Delta f_{IGW})$ appears after JD 90, along with the 1.0 isoline in C_{660} $G_N(\Delta f_{IGW})$, while the 0.5 isoline mirrors the intensification in C_{660} $G_N(\Delta f_{IGW})$ that occurs after JD 110 (Figs. 5a and 7a). Similarly, the 0.05 isoline in the maps of temperature $G_N(\Delta f_{IGW})$ roughly coincides with the onset of elevated Chl $G_N(\Delta f_{IGW})$ at 62 m and 81 m toward the end of this period (Figs. 5b, c and 7b, c). The correspondence is especially striking at 62 m where both maps indicate the intermittent onset of Δf_{IGW} fluctuations which appear around JD 100, dissipate by JD 110 and reappear around JD 128 (Figs. 5b, 7b). At 62 m, the initial appearance of the 0.05 isoline in temperature $G_N(\Delta f_{IGW})$ coincides with the development of stratification (T_Z) greater than 0.005°C/m (Figs. 7b and 10). This T_Z threshold was temporarily reached at the onset of the Δf_{IGW} fluctuations just described, appeared again around JD 120 and was permanently established by JD 130. Interestingly, $\gamma_{XY}(\Delta f_M)$ of temperature with Chl at 62 m (Fig. 9a) appears before and after the first appearance of stratification and the coincident temperature and Chl $G_N(\Delta f_{IGW})$ fluctuations (Figs. 5b, 7b and 10).

d. Period 4 (JD 135–185)

Period 4 is characterized by a marked reduction in mean current speed to 10 cm/s (Table 1) with the current sticks indicating a consistently eastward direction with a series of N–S oscillations observed between JD 150 and JD 165 (Fig. 2a). These current reversals may have been caused by far-field interactions with several eddies that appear near the site in the synoptic temperature map (Fig. 1c). Current and temperature $G_N(\Delta f_M)$ are all low, reflecting the lack of direct mesoscale influence (Fig. 3, 5). However, the current reversals reveal notable meridional gradients in oceanic properties below 60 m. Several $\gamma_{XY}(\Delta f_M)$ maps indicate this, including $\gamma_{XY}(\Delta f_M)$ of meridional current with temperature (Fig. 6b, d)

and $\gamma_{XY}(\Delta f_M)$ of temperature with Chl (Fig. 9). Further evidence for this spatial variability appears in $\gamma_{XY}(\Delta f_M)$ of meridional current with C_{660} and in $\gamma_{XY}(\Delta f_M)$ of dissolved oxygen with both meridional current and temperature (Wiggert, 1995).

The significant reduction in mesoscale influences that occurred during this seven-week period resulted in physical/biological interactions that were predominantly a product of local processes, which allowed for extended observation of DCM evolution. Elevated, broadband Chl $G_N(\Delta f_{IGW})$ at 81 m and 101 m (Figs. 7c, d) and the 0.05 isoline within temperature $G_N(\Delta f_{IGW})$ (Figs. 5c, d) emerge simultaneously as this period begins. As water-column stratification continues to develop (Fig. 10), Δf_{IGW} variability intensifies throughout this period in both temperature and Chl. Despite the noted lack of horizontal advection *via* mesoscale interaction, elevated Chl $G_N(\Delta f_M)$ appears below the mixed layer. This Δf_M variability initiates, and persists, later in time with increasing depth. Specifically, elevated Chl $G_N(\Delta f_M)$ persists through JD 165 at 62 m, appears from JD 110–185 at 81 m and from JD 135–210 at 101 m (Figs. 7b–d). Finally, $\gamma_{XY}(f)$ of temperature with Chl primarily appears Δf_{IGW} at 62 m while at 81 m its essentially restricted to Δf_M (Fig. 9). Taken together, the appearance of elevated Chl $G_N(\Delta f_{IGW})$ and the depth progression of reflect the onset and development of the DCM (see Fig. 7 in Dickey *et al.,* 1993).

e. Period 5 (JD 185–220)

Period 5 is characterized by a series of large-magnitude changes in water-column heat content. Initially, the water column cools by 1°C over JD 185–195 after which temperature increased by up to 5°C at 40 m over JD 195–200 followed by an alternating cooling-heating-cooling cycle that reached 4°C at 62 m over JD 200–220 (Fig. 2b). These changes in observed heat content resulted from the motions of a strong thermal front between a cold-core eddy and warm, entrained Gulf Stream waters (Fig. 1d). This feature's mean speed was 24 cm/s, which is considerably lower than the speeds associated with the mesoscale current fields of periods 1 and 3 (Table 1). However, its passage dominates temperature $G_N(\Delta f_M)$ over the six periods (Fig. 5) and is evident in Z_{ML} time series (Fig. 4), water-column stratification (Fig. 10), current $G_N(\Delta f_M)$ (Figs. 3) and $\gamma_{XY}(\Delta f_M)$ of temperature with dissolved oxygen (values > 0.9; Wiggert, 1995). $\gamma_{XY}(\Delta f_M)$ of temperature with currents shows a transition over JD 202–203 from predominantly meridional to predominantly zonal transport in conjunction with the sharply veering current direction (Figs. 2a and 6).

Chl $G_N(\Delta f_M)$ is inconsistent with depth and highly variable in time, indicating both vertical and horizontal patchiness associated with the front. Elevated Chl $G_N(\Delta f_M)$ at 62 m reflects isolated peaks centered on JD 198 and JD 207 in the time series (Dickey *et al.,* 1993), with deeper Chl $G_N(\Delta f_M)$ values that were low (81 m) to moderate (101 m) (Fig. 7). $\gamma_{XY}(\Delta f_M)$ of temperature with Chl is intermittent at both 62 m and 81 m and principally appears over JD 190–200 and around JD 210 (Fig. 9). These coincide with the two warm-water expressions of the front's passage (Fig. 2b). Maximum temperature $G_N(\Delta f_{IGW})$ coincides with maximum thermal stratification (Fig. 5, 10). Elevated Chl $G_N(\Delta f_{IGW})$

terminates abruptly at all depths with the appearance of this mesoscale feature (Fig. 7). Reestablishment of elevated Chl $G_N(\Delta f_{IGW})$ was not as uniform. At 81 m and 101 m, Δf_{IGW} variability reappears within 5 days, with a broadband expression at 81 m and a band-limited (f_D to f_{SD}) expression at 101 m (Figs. 7c, d). At 62 m, Δf_{IGW} variability reappears around JD 200, coincident with the entrained Gulf Stream waters (Fig. 7b). The discrepancy in timing primarily reflects differences in vertical phytoplankton distribution caused by relative variations in the structure of water-column stratification on either side of the front.

f. Period 6 (JD 220–240)

Period 6 marks a return to local dynamics. Low current and temperature $G_N(\Delta f_M)$ indicate reduced horizontal advection and heat transport (Figs. 3 and 5b–d). Near-surface temperatures begin to decline from their annual maximum while the seasonal thermocline continues to evolve *via* a downward redistribution of heat and a continuing intensification in water-column stratification below the mixed layer (Fig. 10). Thus, it appears that these conditions represent the re-establishment and ongoing evolution of the physical properties observed during period 4 before being disrupted by the mesoscale feature that dominated period 5. A relative cooling occurs at 62 and 81 m over JD 230–233 (Fig. 2b). This event is accentuated in the temperature record by the overall warming of the upper thermocline that occurs during this period and coincides with a decrease in T_Z at 72 m (Figs. 2b, 10 and 11). The reduction in temperature and T_Z is preceded by elevated current shear at 91 m (Fig. 11). Over the six periods presented here, these were the highest current shears observed in the thermocline in the absence of direct mesoscale interaction.

Chl $G_N(\Delta f_M)$ is generally low (Fig. 7), reflecting the steady state production regime that occurs throughout this period (Wiggert, 1995). This is disrupted by a better than threefold increase in Chl within one day at 62 m (Fig. 11). This two-day phytoplankton bloom also appears less prominently at 81 m (Fig. 11 in Dickey *et al.,* 1993). High frequency Chl variability also increased during this bloom. Chl $G_N(\Delta f_{IGW})$ is at a maximum near f_I and f_{SD} and elevated over the entire IGW band at 62 m (Fig. 7b). Temperature $G_N(\Delta f_{IGW})$ is also elevated at 62 m albeit significantly reduced in comparison to period 5 (Fig. 5). However, despite elevated Chl $G_N(\Delta f_{IGW})$ and the internal wave activity indicated in temperature $G_N(\Delta f_{IGW})$ at 62 m, $\gamma_{XY}(\Delta f_{IGW})$ of temperature with Chl was not significant (Fig. 9).

4. Discussion

The six periods described here alternated between advectively and locally derived oceanographic characteristics that were further distinguishable by the presence or absence of water-column stratification. Various combinations of these characteristics, along with the superimposed annual cycle in both physical and biological processes, led to a sequence of physical/biological interaction mechanisms that are summarized to begin this discussion and succinctly encapsulated in Table 1. Following this summary, we compare and contrast

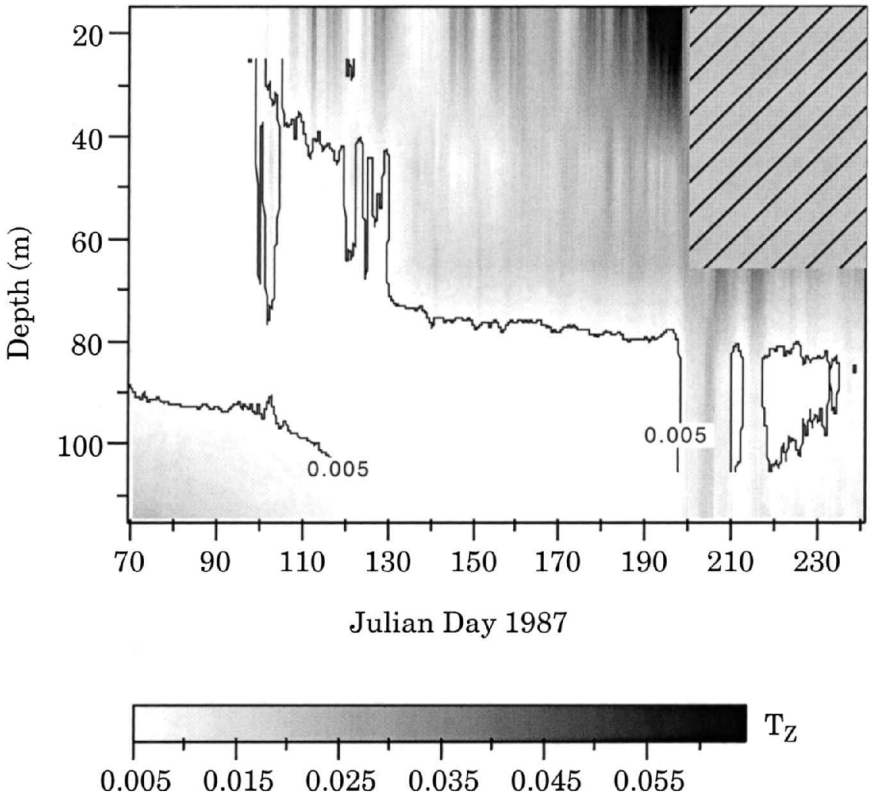

Figure 10. Stratification (T_Z). Units are °C/m. The gray scale threshold is 0.005°C/m. The hatched region is due to missing data at 42 m after JD 200. These data were derived from MVMS temperature time series sampled at seven depths over the upper 120 m of the water column.

the progression of physical/biological interactions that took place once stratification was established, with a more detailed look at periods 4 and 6. These periods exhibit physical processes with spatial and temporal scales consistent with those typical of biological processes. Thus, these periods provide an opportunity to observe a true synergy between the physical and biological components of the pelagic system.

During period 1, large-magnitude, barotropic currents and the intermittent passage of Gulf Stream outbreaks interrupted the typical wintertime regime of deep convective mixing. These outbreaks transported distinct, near-surface bio-optical characteristics past the mooring. Period 2 marks a transition to lower current speeds and deep thermal convection that points to vertical transport of nitrate into the surface waters. $G_N(\Delta f_M)$ for the physical variables indicate relatively homogeneous water mass properties. However, bio-optical $G_N(\Delta f_M)$ at all depths are higher than during period 1 and $\gamma_{XY}(\Delta f_M)$ between zonal current and Chl at 62 m indicates this is due to phytoplankton patch transport (Figs. 7 and 8a). The apparent inconsistency between water mass and phytoplankton patch

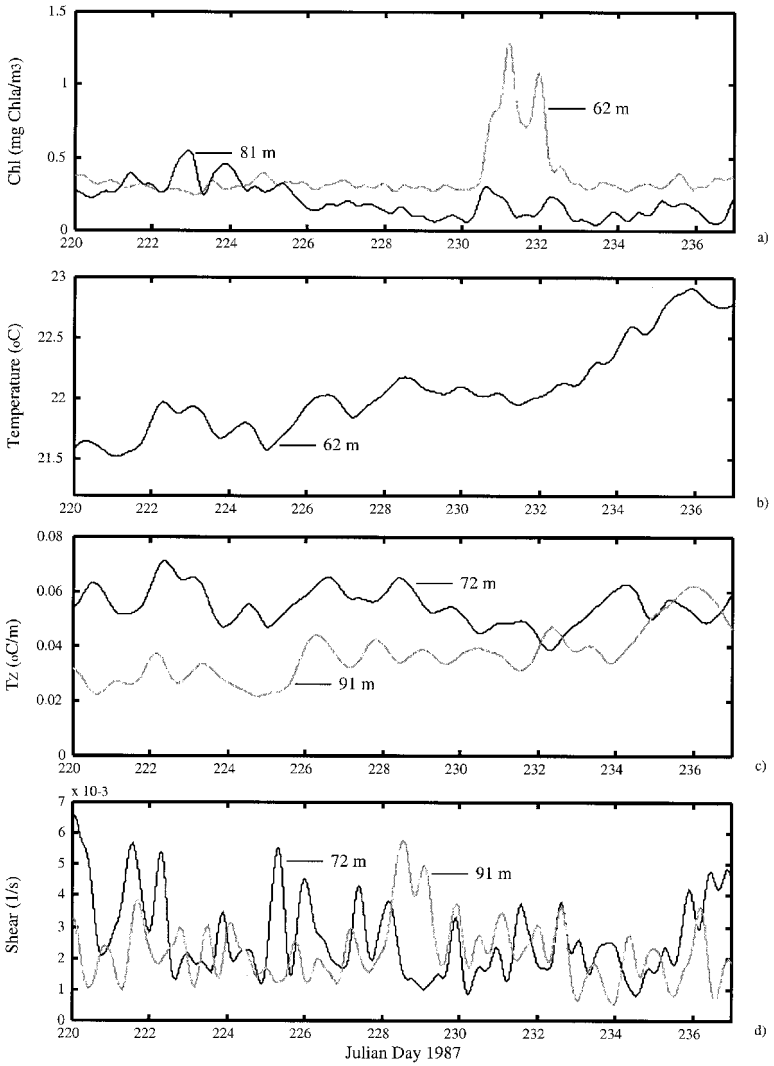

Figure 11. Time series of Chl, temperature and T_Z from period 6. All data shown have been low pass filtered using a 6-hour Butterworth window. (a) Chl data are from 62 and 81 m showing the bloom that occurred between JD 230–232 at 62 m and the slight correspondence with this feature at 81 m. (b) Temperature time series from 62 m illustrating the temperature reduction and interruption in ongoing heating between JD 230–232. (c) Time series of stratification (T_Z) from 71 m and 91 m (based on MVMS thermistors at 62 m, 81 m and 101 m). The reduced values at 71 m between JD 230–232 emphasize the potential for vertical transport of nutrient rich waters from below.

transport may result from horizontal variations in water column stratification that are too insignificant to appear within the physical properties, yet may be sufficient to support larger concentrations of phytoplankton. Over the last few days of the period, a phytoplankton bloom was transported past the site from the east, again indicating that differential

horizontal stratification resulted in notable regional patchiness as well as suggesting that the region's spring bloom was underway.

During period 3, mesoscale advection returned as a dominant process with large-magnitude currents that were barotropic through 160 m (Fig. 2a). These currents exhibited directional veering associated with a mesoscale eddy. This period's other significant occurrence was the initial development of seasonal stratification, which manifests as increasing temperature $G_N(\Delta f_{\mathrm{IGW}})$ due to the internal wave field that formed below the mixed layer (Fig. 5). This developing stratification stimulates phytoplankton growth and the associated vertical structure in Chl which in turn results in the appearance of Chl $G_N(\Delta f_{\mathrm{IGW}})$ due to the internal wave oscillations. Mean current speed during period 4 decreased significantly and was among the lowest values observed (Table 1) while both stratification and temperature $G_N(\Delta f_{\mathrm{IGW}})$ intensified (Figs. 2a, 5 and 10). Thus, interactions between the vertical distribution of phytoplankton and the internal wave field and the evolution of the DCM could be studied with a minimal superposition of horizontal variability. This physical/biological regime governed by local processes was disrupted by a sharp temperature front that moved back and forth across the moored array during period 5. This front's motions appear as the most prominent feature in temperature $G_N(\Delta f_{\mathrm{M}})$ over these six periods (Fig. 5). Both Chl $G_N(\Delta f_{\mathrm{M}})$ and $\gamma_{XY}(\Delta f_{\mathrm{IGW}})$ of temperature with Chl are reduced during this feature's initial appearance (Figs. 7 and 9), most likely because its deep stratification creates a deeper nutricline that leads to nutrient-limited phytoplankton growth. Once this feature leaves the mooring's vicinity, horizontal advection and heat transport return to values observed during period 4 and a physical/biological regime dominated by local dynamics was re-established for period 6. However, insignificant $\gamma_{XY}(\Delta f_{\mathrm{IGW}})$ of temperature with Chl at 62 m and the observed response in Chl to a nutrient injection (Figs. 9 and 11a) indicate that the DCM has progressed below this depth.

Over periods 3 and 4, the seasonal distribution of phytoplankton biomass typifies the classical evolution for an oligotrophic, temperate ocean (see Fig. 7 in Dickey *et al.,* 1993). This starts with the springtime shoaling of the mixed layer triggering a surface phytoplankton bloom followed by the development and evolution of the DCM as mixed layer nutrients become depleted and further near-surface enrichment becomes restricted by stratification (Mann and Lazier, 1991). During the period 3 time frame, the Sargasso Sea's spring bloom has been observed to spread northward with the developing stratification (Bidigare *et al.,* 1990; Siegel *et al.,* 1990). Our analysis reveals persistently elevated Chl $G_N(\Delta f_{\mathrm{M}})$ within the upper seasonal thermocline which reflects biomass fluctuations that are significant within an oligotrophic context and that persist for an extended period (1–2 months). During the highly advective regime of period 3, elevated Chl $G_N(\Delta f_{\mathrm{M}})$ is easily understood in light of the typically observed spring bloom behavior. However, elevated Chl $G_N(\Delta f_{\mathrm{M}})$ continues into the minimally advective regime of period 4 and appears later in time with depth, which mimics the developing stratification (Figs. 7 and 10). Elevated Chl $G_N(\Delta f_{\mathrm{IGW}})$ appears with this elevated Chl $G_N(\Delta f_{\mathrm{M}})$. Their coincident appearance is a robust association that develops and persists at depth through period 4 (Figs. 7c and 7d).

In addition to triggering phytoplankton growth, the developing stratification promotes intensification of the internal wave field, which manifests as increasing temperature $G_N(\Delta f_{\mathrm{IGW}})$ (Fig. 5). We have noted a correspondence between a threshold value of T_Z and the appearance of the 0.05 isoline in temperature $G_N(\Delta f_{\mathrm{IGW}})$ (Figs. 5 and 10). We also observe that this 0.05 isoline coincides with the appearance of elevated Chl $G_N(\Delta f_{\mathrm{IGW}})$ (Figs. 5b and 7b). As 1-D (i.e., local) behavior becomes more prominent and temperature $G_N(\Delta f_{\mathrm{IGW}})$ increases, $\gamma_{XY}(\Delta f_{\mathrm{IGW}})$ between temperature and Chl appears in both Δf_{M} and Δf_{IGW}. Furthermore, the elevated coherence in these two bands shows a strong temporal correspondence (Fig. 9).

These observations of high frequency variability in DCM evolution stimulated a more detailed look at the time series in order to better understand what specific processes caused these Δf_{M} and Δf_{IGW} coherence features. To this end, a 5-day subset (JD 145–150) of temperature and Chl time series from 62 m and 81 m were partitioned into low and high frequency fluctuations (Fig. 12). The low-passed time series show that biomass fluctuations are directly associated with temperature drops of 0.2–0.4°C. The 62 m Chl is consistently lower in magnitude than the 81 m Chl and shows episodic biomass increases for only the two lowest temperature excursions (JD 145.6 and JD 149). Similar increases are observed at 81 m as well as two additional peaks (JD 147 and 148) both of which appear as a doubling in Chl (0.6–1.2 mg Chl a/m^3). Since three of these peaks occurred near local midnight on successive days (JD 147, 148 and 149) and this period was subjected to minimal horizontal advection, we ascribe these episodic increases in Chl to vertical transport of the DCM by IGW oscillations rather than in-situ growth. It is apparent in these low frequency data that the principal component of these oscillations is the internal tide. Based on mean T_Z (0.02°C/m), the oscillation amplitude ranges from 20 to 15 m at depths of 62 m and 81 m, respectively.

The frequency partitioned data (Fig. 12) reinforce the association between Δf_{M} and Δf_{IGW} variability observed in the maps of Chl $G_N(f)$ and temperature/Chl $\gamma_{XY}(f)$ (Figs. 7 and 9). At 62 m, the largest low-passed variations in temperature are ~0.2°C. Except on JD 145.7, the associated biomass variations are $\leq$0.15 mg Chl a/m^3, which represent an increase of ~30%. Low-passed temperature variations of similar magnitude are observed at 81 m. However, the associated variation in biomass is consistently ~0.6 mg Chl a/m^3, which represents an increase of 100% (Fig. 12). The fact that biomass variations at 81 m are consistently and significantly greater than those at 62 m, despite similar internal wave forcing, may reflect the proximity of the nutricline and the DCM to the 81 m MVMS. Equivalently, the relative magnitudes of these low frequency Chl variations may indicate that phytoplankton growth at 62 m is nutrient limited and principally dependent upon recycled nutrients.

Over the entire 5-day period, the high frequency 62 m temperature and Chl signals vary such that a decrease in temperature coincides with an increase in Chl. This is generally true at 81 m as well (Fig. 12). However, there are five instances, lasting 6–24 hours, during which high frequency temperature and Chl from 81 m vary directly (Fig. 12d). Without

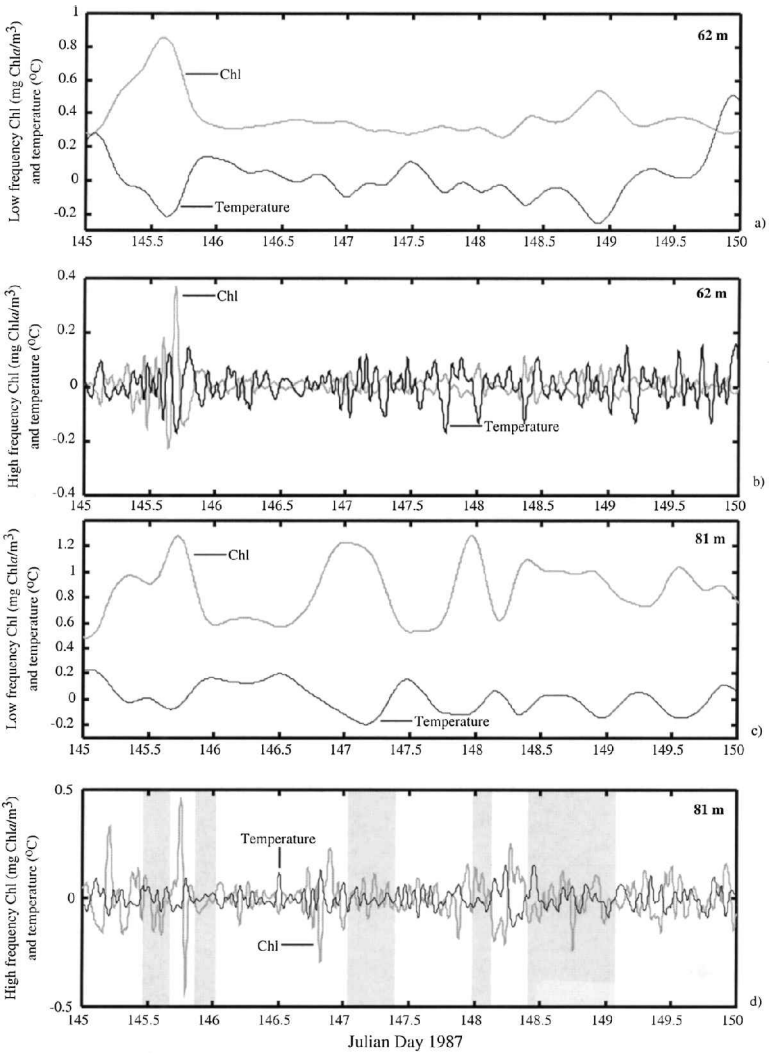

Figure 12. Superimposed Chl and temperature time series from 62 m (a, b) and 81 m (c, d) for JD 145–150. The low frequency time series (a, c) were filtered using a 6 hour Butterworth filter. The high frequency time series (b, c) were band passed to include variability with characteristic time scales of 1–6 hours, thus removing prominent variability at f_D, f_I and f_{SD}. The high frequency data have had the means removed to emphasize the oscillations and to bring out the phase relation between the two variables. The low frequency temperature signal has also been de-meaned to emphasize temperature changes. Periods for which the high frequency Chl and temperature signals vary directly are denoted with gray shading. Within the text, 'direct variation' refers to two signals that increase or decrease simultaneously. Similarly, 'inverse variation' refers to instances when an increase in one signal precisely coincides with a decrease in the other.

coincident time series of salinity, it could be argued that these changes result from temperature inversions within interleaving water masses. However, evidence of interleaving in the upper 200 m appears in neither the CTD casts from the deployment/recovery cruise 2 weeks prior to these time series nor in historical data (Trask *et al.,* 1982). Therefore, we attribute these changes in the relationship between temperature and Chl to vertical structure in the biomass distribution, not salinity-compensated vertical temperature structure.

The five instances of direct variation between high frequency temperature and Chl generally coincide with minimum temperatures in the low-passed time series and low values of T_Z at depth (Figs. 10 and 12c). In addition, local minima in time series of 91 m T_Z coincide with these five periods of direct variation. Four of these minima are <0.1°C/m and two (prior to the second and third occurrences) approach 0.0°C/m (not shown). These T_Z values are strong indicators of vertical mixing which, in turn, suggests episodic transport of nutrients into the base of the euphotic zone. We interpret the change in phasing between the high frequency temperature and Chl observations at 81 m as a sequence of episodic transitions from nutrient limited growth (the nominal condition) to light limited growth in conjunction with the nutrient injections. In other words, higher Chl coinciding with lower temperature (inverse variation) indicates greater nutrient limitation at shallower depths, whereas higher Chl coinciding with higher temperature (direct variation) associated with a nutrient injection reflects the impact of vertical PAR attenuation on photosynthetic rates. The phytoplankton growth that is stimulated by these nutrient injections contributes to maintaining the DCM, which is observed between 80 and 100 m throughout period 4 (see Fig. 18 in Dickey *et al.,* 1993).

The strong thermal front between the cold-core eddy and its entrained Gulf Stream waters served to define the extent of period 5 while it disrupted the predominantly local physical and biological processes that occurred during the surrounding periods. However, this mesoscale feature provided an opportunity to observe the biological response to physical processes unique to such a frontal system. Elevated Chl $G_N(\Delta f_M)$ appears at 62 m after JD 190. This marks a doubling in Chl that persisted for 2 days and was located on the warm side of the eddy/outbreak front (Figs. 1d, 2b, 7b and 10). This implies either that the biomass was recently formed or that there was a mechanism in force that was capable of continuously supplying nutrients. The combination of a strong thermal front and maximal temperature $G_N(\Delta f_{IGW})$ (Figs. 2b, 5) suggests that the elevated biomass was supported by vertical nutrient transport driven by near-inertial internal wave intensification along the warm side of the mesoscale front (Kunze and Sanford, 1984; Kunze, 1985). Such an intensification is indicated by the order of magnitude increase that appears in time series of $G_N(f_I)$ (not shown). The broadband increase in current and temperature $G_N(\Delta f_{IGW})$ (Figs. 3, 5) further suggests that this near-inertial energy was partially redistributed to higher frequencies *via* wave-wave interaction which would lead to elevated internal wave energy, more frequent wave breaking and enhanced turbulent mixing (Kunze and Sanford, 1984). These physical processes would provide a mechanism for vertical nutrient transport that

could result in the Chl increase observed at 62 m. Furthermore, an entrainment bloom would reestablish the vertical biomass gradient that is indicated by increased Chl $G_N(\Delta f_{IGW})$ (Figs. 7b and c). The feature in $\gamma_{XY}(f_I)$ between temperature and Chl at 81 m that appears over the first two-thirds of this period points to such an interaction (Fig. 9b). A similar biomass enhancement related to frontal dynamics occurred during the Biowatt experiment's third deployment and was the focus of a detailed study of this mechanism (Granata *et al.,* 1995).

Period 6 sees the re-establishment of locally driven physical/biological interaction. Current velocities and stratification return to conditions observed toward the end of period 4 (Figs. 2a and 10), with the onset of mixed layer deepening as surface heating decreases and downward redistribution of water-column heat content commences (Figs. 2b and 4). The decrease in horizontal advection appears as reduced current and temperature $G_N(\Delta f_M)$ and a lack of $\gamma_{XY}(\Delta f_M)$ between currents and temperature (Figs. 3, 5 and 6). The highest values of temperature $G_N(\Delta f_{IGW})$ are observed at 62 m during this period, which is consistent with the observed redistribution of water-column heat content (Figs. 2b and 5b). Chl $G_N(\Delta f_{IGW})$ is also elevated, yet $\gamma_{XY}(\Delta f_{IGW})$ between temperature and Chl is not significant (Figs. 5b, 7a, 9a) and the relation between high-passed temperature and Chl time series is inconsistent (not shown). This indicates that the vertical distribution of Chl is no longer directly related to temperature or, *via* proxy, nitrate (Figs. 5b, 7b and 9a), as was true during period 4. It is possible that elevated Chl $G_N(\Delta f_{IGW})$ results from horizontal transport of phytoplankton patchiness by short term currents. $\gamma_{XY}(\Delta f_{IGW})$ of currents with Chl does not indicate such behavior (Fig. 8) although it is quite likely that over short time periods, the relationship between these two variables would be non-linear which would preclude manifestation within the coherence maps and would negatively impact $\gamma_{XY}(\Delta f_{IGW})$ between temperature and Chl.

Alternatively, the vertical Chl distribution may be based on the availability of regenerated nutrients, which could be determined by a variety of processes, such as heterotrophic grazing, diffusion and shear induced mixing (McCarthy and Goldman, 1979). These would tend to result in a nonlinear relation between temperature and Chl, again resulting in an absence of significant high frequency coherence between these variables. The latter interpretation is consistent with the observed subsidence of the DCM beyond 62 m and a transition to recycled production. Further evidence for such a transition in nutrient resources is provided by HPLC measurements obtained just prior to period 4 and just after period 6 (Bidigare *et al.,* 1990). While total algal biomass was essentially constant, a shift in community structure occurred. Areal concentrations of pigment biomarker associated with specific phytoplankton species indicated a 2.5 fold decrease in diatom biomass, a 1.5 fold increase in prochlorophyte biomass and the appearance of significant dinoflagellate biomass (Bidigare and Ondrusek, 1988). This shift in phytoplankton speciation was accompanied by a deepening of the nutricline from 70 m on JD 138 to >100 m on JD 235 (Marra *et al.,* 1992).

This recycled production regime was disrupted by a phytoplankton bloom at 62 m which

appeared as elevated Chl $G_N(\Delta f_M)$ and increased Chl concentration (JD 230–232, Figs. 7b and 11a). This coincided with decreased temperature at 62 m and decreased T_Z at 72 m and occurred just after maximal current shear (for non-advective periods) at 91 m (Fig. 11b–d) and 110 m (not shown). These physical characteristics, in conjunction with minimal horizontal advection (Figs. 2a, 3), indicate that the bloom occurred in response to a nutrient injection caused by shear-induced mixing associated with internal wave breaking. Chl concentration at 81 m dropped below 0.1 mg Chl *a*/m^3 in conjunction with the elevated shear and the reduced deep stratification (Fig. 11). The bloom at 62 m and the reduction in Chl at 81 m both result from this mixing event, with the transport of nitrate to higher light levels triggering the bloom and the downward mixing of Chl resulting in the observed dilution at 81 m.

5. Conclusions

The maps of normalized spectral variance ($G_N(f)$) and spectral coherence ($\gamma_{XY}(f)$) presented here were created in order to quantify the temporal evolution of spectral variance that was obvious in deployment averaged spectra (Wiggert, 1995). Mesoscale features that could be easily discerned within the time series are well represented in these maps. However, temporal variability is difficult to isolate in the time series for frequencies $>f_I$. These maps' main contribution to our analysis of these high-resolution, colocated physical and bio-optical time series was to reveal temporal changes in variance at these higher frequencies. For instance, within Δf_{IGW}, we noted a strong correspondence between the 0.05 isoline in temperature $G_N(\Delta f_{IGW})$ and the depicted threshold of T_Z. We also found an intriguing correspondence between elevated Chl $G_N(\Delta f_M)$ and elevated Chl $G_N(\Delta f_{IGW})$ that led to a closer look at the time series and some insights on the development and maintenance of the deep chlorophyll maximum (DCM). Using these $G_N(f)$ maps, along with similar temporal distributions of $\gamma_{XY}(f)$ between different measurements, we could identify specific physical/biological interaction mechanisms and resolve their seasonal evolution over the full frequency bandwidth contained within the observations.

The seasonal evolution illustrates a succession of characteristic scales within the biomass distributions. Of the periods dominated by mesoscale activity, the observed spring phytoplankton bloom at the end of period 2 provides a constrained event for quantifying temporal and spatial scales. Current speeds range from 15 to 18 cm/s toward the southwest and the duration of the bloom's passage ranges from 2.5 to 2.9 days over the upper 40 m. This indicates a 'bulk' patch scale of 23 to 30 km that decreases with depth. This bloom was contained within a Gulf Stream outbreak that was bio-optically distinct from Sargasso Sea waters. Permanent stratification develops and intensifies through periods 3 and 4. Vertical structure in the bio-optical measurements develops coincidentally and high frequency Chl variability propagates downward, following the deepening stratification. The $\gamma_{XY}(f)$ maps also indicate significant phytoplankton patchiness during periods 2 and 3 that we attribute to slight horizontal differences in stratification and environmental conditions primed for the region's bloom.

It is clear that stratification is a cornerstone of the pelagic ecosystem *via* its impact on the temporal and spatial scales of vertical mixing within the euphotic zone and the attendant effect on phytoplankton growth rates, accumulation and patchiness (Harris, 1986; Valiela, 1995). Towed studies have consistently been confounded by the inability to unambiguously determine scales of horizontal patchiness in the presence of internal wave oscillations (Denman and Platt, 1975). With our moored data it was possible, to some extent, to partition patchiness into horizontally and vertically derived components. This partitioning clearly indicates that the dominant physical/biological interaction mechanism governing ecosystem patch dynamics is determined by the intensity of water-column stratification and the associated IGW field versus the magnitude of horizontal advection associated with mesoscale activity. With decreasing horizontal advection and developing stratification, the temporal and spatial scales of the dominant physical processes shift from Δf_M variability, ($\approx$5 days and $\approx$50 km in the horizontal), to IGW variability, ($\approx$6 hours and $\approx$10 m in the vertical). This transition allows biological variability to shift from passive transport within mesoscale phenomena to a complex synergy of horizontal transport and vertical oscillations (associated with the IGW field) and direct physiological response to environmental fluctuations associated with these oscillations (Denman and Powell, 1984; Holloway, 1984).

Our time series reveal the DCM's response to the onset and evolution of stratification within the upper thermocline at time scales that range from seasonal to intraday. The seasonal evolution of the DCM reflects the utilization of nutrients within the euphotic zone such that, with time, the DCM propagates downward in the water column. This coincides with the downward penetration of increasing stratification that restricts the depth to which ongoing entrainment of nitrate into the euphotic zone can occur. This seasonal behavior is consistent with classical explanations of DCM evolution (e.g., Wolf and Woods, 1988). With the aid of the $G_N(f)$ and $\gamma_{XY}(f)$ maps of the Chl and temperature measurements, we could distinguish evidence of frequent mixing events that stimulated phytoplankton growth. We attribute these mixing events to breaking internal waves and their repeated occurrence over an extended time period (every 2 to 4 days over 6 to 8 weeks) resulted in temporally coincident manifestations of elevated Chl $G_N(f)$, in both Δf_M and Δf_{IGW}, as well as $\gamma_{XY}(\Delta f_{IGW})$ between temperature and Chl. Their appearance within these maps led to a careful examination of the time series over the appropriate period and aided our interpretation of these moored observations of the processes that helped maintain the DCM during its seasonal evolution.

Acknowledgments. This research was sponsored by the Office of Naval Research as part of the Biowatt program (contracts N00014-87-K0084 (TDD) and N00014-86-K0204 (JM)). JDW was supported during manuscript preparation by USRA contract NAS5-32484. Derek Manov, Miguel Maccio, John Scott, Ivars Bitte and Larry Sullivan provided technical assistance during the Biowatt experiment. Mike Hamilton provided assistance with the data. The manuscript has benefited from the comments of Libe Washburn, Jim Kremer and Burt Jones. The comments of M. Lewis and several anonymous reviewers significantly improved this manuscript and were greatly appreciated.

REFERENCES

Bendat, J. S. and A. G. Piersol. 1986. Random Data: Analysis and Measurement Procedure. Wiley-Interscience,NY, 566 pp.

Bidigare, R. R., J. Marra, T. D. Dickey, R. Iturriaga, K. S. Baker, R. C. Smith and H. Pak. 1990. Evidence for phytoplankton succession and chromatic adaptation in the Sargasso Sea during springtime 1985. Mar. Ecol. Prog. Ser., *60,* 113–122.

Bidigare, R. R. and M. E. Ondrusek. 1988. Biowatt II Data Report. Department of Oceanography, Texas A&M University, College Station, 49 pp.

Bloomfield, P. 1976. Fourier Analysis of Time Series: An Introduction, Wiley and Sons, NY, 258 pp.

Cornillon, P., D. Evans and W. Large. 1986. Warm outbreaks of the Gulf Stream into the Sargasso Sea. J. Geophys. Res., *91,* 6583–6596.

Denman, K. L. 1976. Covariability of chlorophyll and temperature in the sea. Deep-Sea Res., *23,* 539–550.

Denman, K. L. and A. E. Gargett. 1983. Time and space scales of vertical mixing and advection of phytoplankton in the upper ocean. Limnol. Oceanogr., *28,* 801–815.

Denman, K. L. and J. Marra. 1986. Modelling the time dependent photoadaptation of phytoplankton to fluctuating light, *in* Marine Interfaces Ecohydrodynamics, J.C.J. Nihoul, ed., Elsevier Oceanography Series., Vol. 42, Elsevier, NY, 690 pp.

Denman, K. L. and T. Platt. 1975. Coherences in the horizontal distributions of phytoplankton and temperature in the upper ocean. Mem. Soc. Roy. des Sciences de Liege, *6,* 19–30.

Denman, K. L. and T. M. Powell. 1984. Effects of physical processes on planktonic ecosystems in the coastal ocean. Oceanogr. Mar. Biol. Ann. Rev., *22,* 125–168.

Dickey, T. D., T. Granata, J. Marra, C. Langdon, J. Wiggert, Z. Chai, M. Hamilton, J. Vasquez, M. Stramska, R. Bidigare and D. Siegel. 1993. Seasonal variability of bio-optical and physical properties in the Sargasso Sea. J. Geophys. Res., *98,* 865–898.

Dickey, T. D., J. Marra, T. Granata, C. Langdon, M. Hamilton, J. Wiggert, D. Siegel and A. Bratkovich. 1991. Concurrent high resolution bio-optical and physical time series observations in the Sargasso Sea during the spring of 1987. J. Geophys. Res., *96,* 8643–8664.

Dickey, T. D. and J. J. Simpson. 1983. The influence of optical water type on the diurnal response of the upper ocean. Tellus, *35,* 142–154.

Eriksen, C. C. 1988. Variability in the upper-ocean internal wave field at a Sargasso Sea site. J. Phys. Oceanogr., *18,* 1495–1513.

Fasham, M. J. R. and P. R. Pugh. 1976. Observations of horizontal coherence of chlorophyll *a* and temperature. Deep-Sea Res., *23,* 527–538.

Franks, P. J. S. and J. Marra. 1994. A simple new formulation for phytoplankton photoresponse and an application in a wind-driven mixed-layer model. Mar. Ecol. Prog. Ser., *111,* 143–153.

García-Moliner, G. and J. A. Yoder. 1994. Variability in pigment concentration in warm-core rings as determined by coastal zone color scanner satellite imagery from the Mid-Atlantic Bight. J. Geophys. Res., *99,* 14,277–14,290.

Granata, T., J. Wiggert and T. Dickey. 1995. Trapped, near-inertial waves and enhanced chlorophyll distributions. J. Geophys. Res., *100,* 20793–20804.

Gregg, M. C. and M. G. Briscoe. 1979. Internal waves, finestructure, microstructure and mixing in the ocean. Rev. Geophys. Space Phys., *17,* 1524–1548.

Harris, F. J. 1978. On the use of windows for harmonic analysis with the discrete Fourier transform. Proceedings of the IEEE, *66,* 51–83.

Harris, G. P. 1986. Phytoplankton Ecology: Structure, Function and Fluctuation. Chapman and Hall, NY, 384 pp.

Haury, L. R., P. H. Wiebe, M. H. Orr and M. G. Briscoe. 1983. Tidally generated high-frequency internal wave packets and their effects on plankton in Massachusetts Bay. J. Mar. Res., *41,* 65–112.

Hitchcock, G. L., C. Langdon and T. J. Smayda. 1985. Seasonal variations in the phytoplankton biomass and productivity of a warm-core Gulf Stream ring. Deep-Sea Res., *32,* 1287–1300.

Holloway, G. 1984. Effects of velocity fluctuations on vertical distributions of phytoplankton. J. Mar. Res., *42,* 559–571.

Holloway, G. and K. Denman. 1989. Influence of internal waves on primary production. J. Plankton Res., *11,* 409–413.

Jamart, B. M., D. F. Winter, K. Banse, G. C. Anderson and R. K. Lam. 1977. A theoretical study of phytoplankton growth and nutrient distribution in the Pacific Ocean off the northwestern U.S. coast. Deep-Sea Res., *24,* 753–773.

Joyce, T. M. 1984. Velocity and hydrographic structure of a Gulf Stream warm-core ring. J. Phys. Oceanogr., *14,* 936–947.

Kahru, M. 1983. Phytoplankton patchiness generated by long internal waves: A model. Mar. Ecol. Prog. Ser., *10,* 111–117.

Kamykowski, D. 1974. Possible interactions between phytoplankton and semidiurnal internal tides. J. Mar. Res., *32,* 67–89.

Kunze, E. 1985. Near-inertial wave propagation in geostrophic shear. J. Phys. Oceanogr., *15,* 544–565.

Kunze, E. and T. B. Sanford. 1984. Observations of near-inertial waves in a front. J. Phys. Oceanogr., *14,* 566–581.

Lande, R. and A. M. Wood. 1987. Suspension times of particles in the upper ocean. Deep-Sea Res., *34,* 61–72.

Leaman, K. D. and T. B. Sanford. 1975. Vertical energy propagation of internal waves: A vector spectral analysis of velocity profiles. J. Geophys. Res., *80,* 1975–1978.

Lewis, M. R., J. J. Cullen and T. Platt. 1983. Phytoplankton and thermal structure in the upper ocean: Consequences of nonuniformity in chlorophyll profile. J. Geophys. Res., *88,* 2565–2570.

—— 1984. Relationships between vertical mixing and photoadaptation of phytoplankton: similarity criteria. Mar. Ecol. Prog. Ser., *15,* 141–149.

Mann, K. H. and J. R. N. Lazier. 1991. Dynamics of Marine Ecosystems: Biological-Physical Interactions in the Ocean. Blackwell Science, Cambridge, MA, 466 pp.

Marra, J. 1978. Phytoplankton photosynthetic response to vertical movement in a mixed layer. Mar. Biol., *46,* 203–208.

Marra, J., T. Dickey, W. S. Chamberlin, C. Ho, T. Granata, D. A. Kiefer, C. Langdon, R. Smith, K. Baker, R. Bidigare and M. Hamilton. 1992. The estimation of seasonal primary production from moored optical sensors in the Sargasso Sea. J. Geophys. Res., *97,* 7399–7412.

McCarthy, J. J. and J. C. Goldman. 1979. Nitrogenous nutrition of marine phytoplankton in nutrient-depleted waters. Science, *203,* 670–672.

McGillicuddy, D. J., R. Johnson, D. A. Siegel, A. F. Michaels, N. R. Bates and A. H. Knap. 1999. Mesoscale variations of biogeochemical properties in the Sargasso Sea. J. Geophys. Res., *104,* 13381–13394.

McGillicuddy, D. J., Jr., A. R. Robinson, D. A. Siegel, H. W. Jannasch, R. Johnson, T. D. Dickey, J. McNeil, A. F. Michaels and A. H. Knap. 1998. Influence of mesoscale eddies on new production in the Sargasso Sea. Nature, *394,* 263–266.

McNeil, J. D., H. W. Jannasch, T. Dickey, D. McGillicuddy, M. Brzezinski and C. M. Sakamoto. 1999. New chemical, bio-optical and physical observations of upper ocean response to the passage of a mesoscale eddy off Bermuda. J. Geophys. Res., *104,* 15537–15548.

Morel, A. and D. Antoine. 1994. Heating rate within the upper ocean in relation to its bio-optical state. J. Phys. Oceanogr., *24,* 1652–1665.

Nelson, D. M., J. J. McCarthy, T. M. Joyce and H. W. Ducklow. 1989. Enhanced near-surface nutrient variability and new production resulting from the frictional decay of a Gulf Stream warm-core ring. Deep-Sea Res., *36,* 705–714.

Platt, T. 1977. Spectral analysis of spatial structure in phytoplankton populations. *in* Spatial Pattern in Plankton Communities, J. Steele, ed., NATO Conference Series Series IV: Marine Sciences. Vol. 3, Plenum Press, NY, 470 pp.

Prezelin, B. B., M. M. Tilzer, O. Schonfield and C. Haese. 1991. The control of the production process of phytoplankton by the physical structure of the aquatic environment with special reference to its optical properties. Aquat. Sci., *53,* 136–186.

Siegel, D. A., R. Iturriaga, R. R. Bidigare, R. C. Smith, H. Pak, T. D. Dickey, J. Marra and K. S. Baker. 1990. Meridional variations of the springtime phytoplankton community in the Sargasso Sea. J. Mar. Res., *48,* 379–412.

Siegel, D. A., D. J. McGillicuddy and E. A. Fields. 1999. Mesoscale eddies, satellite altimetry, and new production in the Sargasso Sea. J. Geophys. Res., *104,* 13359–13379.

Smith, R. C. and K. S. Baker. 1985. Spatial and temporal patterns in pigment biomass in Gulf Stream warm-core ring 82B and its environs. J. Geophys. Res., *90,* 8859–8870.

Stramska, M. and T. D. Dickey. 1994. Modeling phytoplankton dynamics in the northeast Atlantic during the initiation of the spring bloom. J. Geophys. Res., *99,* 10,241–10,253.

Sverdrup, H. U. 1953. On condition of vernal blooming of phytoplankton. J. Cons. Exp. Mer., *18,* 287–295.

Townsend, A. A. 1976. The Structure of Turbulent Shear Flow. Cambridge University Press, Cambridge, 429 pp.

Trask, R. P., M. G. Briscoe and N. J. Pennington. 1982. Long term upper ocean study (LOTUS): A summary of the historical data and engineering test data. Woods Hole Oceanographic Institution, Woods Hole, MA, 107 pp.

Valiela, I. 1995. Marine Ecological Processes. Springer-Verlag, NY, 686 pp.

Varela, R. A., A. Cruzado, J. Tintoré and E. G. Ladona. 1992. Modeling the deep-chlorophyll maximum: A coupled physical-biological approach. J. Mar. Res., *50,* 441–463.

Wiggert, J. D. 1995. Analysis of High Resolution Physical/Bio-optical Moored Time Series and Comparison to a 1-D Interdisciplinary Ocean Model. PhD. Thesis, University of Southern California, 263 pp.

Wolf, K. U. and J. D. Woods. 1988. Lagrangian simulation of primary production in the physical environment—The deep chlorophyll maximum and nutricline, *in* Toward a Theory on Biological-Physical Interactions in the World Ocean, B. J. Rothschild, ed., Kluwer Academic Publishers, Dordrech, Netherlands, 51–70.

Received: *22 December, 1998;* revised: *8 November, 1999.*